

Article

Optimisation of Solid-State Batteries: A Modelling Approach to Battery Design

Jan Felix Plumeyer * , Friedrich Moesle , Sebastian Wolf , Henrik Born, Heiner Hans Heimes  and Achim Kampker 

Production Engineering of E-Mobility Components (PEM), RWTH Aachen University, 52072 Aachen, Germany; friedrich.moesle@rwth-aachen.de (F.M.)

* Correspondence: j.plumeyer@pem.rwth-aachen.de

Abstract: Solid-state batteries (SSBs) present a promising advancement in energy storage technology, with the potential to achieve higher energy densities and enhanced safety compared to conventional lithium-ion batteries. However, their commercialisation is hindered by technical limitations and fragmented research efforts that predominantly focus on materials or individual performance parameters. This narrow scope limits SSB design and optimisation, potentially delaying the transition to commercial cells. Addressing these challenges requires a systematic framework that integrates key design and performance considerations. This study introduces a modelling framework that addresses these challenges by offering a systematic approach to SSB design. The model streamlines the design process by enabling users to define material selections and cell configurations while calculating key performance indicators (KPIs), such as energy density, power density, and resistance, as well as the specifications required for cell manufacturing. A material compatibility validation feature ensures appropriate selection of anode, cathode, and electrolyte materials, while an integrated sensitivity analysis (SA) function identifies critical design parameters for performance optimisation. The model's accuracy and applicability were validated through comparisons with experimental data, established design frameworks, and the reverse-engineering of commercial SSB prototypes. Results show that the model predicts energy densities within a $\pm 4\%$ deviation in most cases. Additionally, the application of SA highlights its effectiveness in refining design parameters and optimising cell configurations. Despite certain limitations, the model remains a valuable tool in the early stages of battery concept development. It offers researchers and industry professionals a practical means to assess the feasibility of SSB designs and support future scale-up and industrialisation efforts.



Academic Editor: Hirotoshi Yamada

Received: 9 February 2025

Revised: 4 April 2025

Accepted: 7 April 2025

Published: 14 April 2025

Citation: Plumeyer, J.F.; Moesle, F.; Wolf, S.; Born, H.; Heimes, H.H.; Kampker, A. Optimisation of Solid-State Batteries: A Modelling Approach to Battery Design. *Batteries* **2025**, *11*, 153. <https://doi.org/10.3390/batteries11040153>

Copyright: © 2025 by the authors. Licensee MDPI, Basel, Switzerland. This article is an open access article distributed under the terms and conditions of the Creative Commons Attribution (CC BY) license (<https://creativecommons.org/licenses/by/4.0/>).

Keywords: solid-state batteries; battery development process; model-based method; design toolkit; model framework; battery design optimisation; energy density estimation; sensitivity analysis; material compatibility; industrialisation; scale-up

1. Introduction

The urgent need to mitigate climate change has driven a shift towards electrification across various sectors, with renewable energy sources playing a central role in powering this transition. However, achieving sustainable and efficient large-scale electrification depends heavily on the development of advanced energy storage systems [1]. Currently, lithium-ion batteries (LIBs) serve as the primary solution across applications such as electric vehicles, residential energy storage, and industrial uses. Although LIB technology has

reached a high level of maturity, it faces several critical limitations, including moderate energy density constrained by material chemistry, safety issues related to flammable liquid electrolytes (LEs), and limited operational temperature ranges that restrict charge rates and overall charging speed [2,3].

In response to these challenges, solid-state batteries (SSBs) have emerged as a promising alternative, offering enhanced energy density, improved safety, and therefore broader application range. SSBs replace the LE with a non-flammable solid electrolyte (SE) and typically use high-capacity materials like lithium metal (Li-metal) anodes, enabling compact designs and extended range [4–6]. These characteristics give SSBs notable advantages over LIBs. Despite this potential, SSB commercialisation remains hindered by complex technical challenges [7–10]. Research is often fragmented, with studies primarily focusing on isolated material properties or specific performance parameters, limiting comprehensive insights into SSB design and optimisation [11]. This narrow focus restricts decision-making in battery development and could delay the transition from laboratory-scale prototypes to viable market-ready products [8,12–14].

To gain deeper insights into overcoming these challenges and advancing SSB development, it is beneficial to develop an understanding of the methodology of battery design and development [15]. This methodology offers a structured framework for navigating the design and development stages [16], which is analogous to broader product development processes [17,18]. The design and development process is depicted in Figure 1.



Figure 1. Battery development process based on the product development process.

The process begins with the pre-development phase, where specific requirements are systematically determined based on the intended application of the battery [16–18]. During this phase, key performance indicators (KPIs), including energy density, safety, cycle life, charging capabilities, and cost, are carefully defined [8,11]. These KPIs serve as essential benchmarks, directing the subsequent phases of battery design to ensure alignment with performance goals and application-specific demands [11].

During the development phase, the conceptual framework is transformed into a detailed and refined design [18]. At this stage, models play a crucial role in accelerating the product design process [16,18–20]. By enabling simulations of various configurations

and providing a comprehensive analysis of their performance, these models support an efficient and systematic exploration of design trade-offs [12,20,21]. Furthermore, they aid in optimising material selection and assessing design feasibility under different operational constraints [12,20,21]. The resulting design can either be implemented as a prototype for practical evaluation or further optimised using advanced modelling techniques to enhance performance metrics [19,20,22,23].

While many SSB modelling approaches have been developed, they primarily focus on understanding fundamental processes rather than offering comprehensive tools for practical battery design and optimisation [12]. Significant efforts in SSB modelling have centred on multiphysics approaches to capture the complex interactions governing battery performance [24]. These models primarily focus on three key areas [25]. Table 1 provides an overview of recent modelling approaches.

First, ionic and electronic transport is modelled to describe the movement of ions and electrons within electrodes and electrolytes, which is essential for understanding conductivity and diffusion transport mechanisms [26–28]. Secondly, the electrode/electrolyte interface is characterised by models that aim to elucidate the mechanisms and interactions at the interface, including structural changes, charge transfer processes, and the stability of material contacts [15,29,30]. Third, multiphysics coupling integrates electrochemical and mechanical behaviours, offering insights to accelerate the prediction of performance-limiting factors, such as overpotentials, interfacial reactions, and inactive particles [31,32].

Table 1. Modelling approaches for various battery types and chemistries in existing research.

Model Type	Ref.	Battery Type	Battery Chemistry
Empirical design and estimation model	Knehr (2022) [21] Dixit (2022) [12]	LIB SSB	Multiple chemistries Multiple chemistries
Multiphysics model	Li (2024) [27]	SSB	Li-Si LPSC NCM811
	Scheller (2024) [15]	SSB	Polymer interlayer LLZO
	Fu (2023) [26]	SSB	Multiple chemistries
	Vadhva (2022) [29]	SSB	Li-Si LPN LCO
	Deng (2021) [30]	SSB	Li LPO LCO
	Raijmakers (2020) [31]	SSB	Li LPN LCO
	Park (2020) [32]	SSB	Li LPSC NCM715
	Sangrós (2020) [28]	SSB	Li PEO-LiTFSi LFP
Mechanical model	Sultanova (2021) [33]	SSB	Polymer-based cathodes

On the other hand, single-physics models focus on specific aspects of battery behaviour, such as mechanical influences, providing detailed insights into isolated phenomena. For instance, microstructural effects are addressed using mechanical models, such as those proposed by Sultanova et al., which account for factors including tortuosity, particle interactions, and microstructural variability that influence transport properties [33].

While these models are relatively accurate in predicting specific characteristics or aspects of SSB mechanisms, their general applicability is inherently limited. This limitation stems from their focus on micro- and meso-scale processes, such as ionic transport, interfacial kinetics, or mechanical stress, which are often modelled in isolation [34]. Although such focused approaches yield valuable insights into individual mechanisms, they fail to capture the interconnected nature of the complete battery system [8] (p 82). This issue is further exacerbated by the fact that certain models are designed for single, pre-specified battery chemistries [27–33]. For example, a model optimised for Li-Si | LPSC | NCM811 chemistry may deliver highly accurate predictions for that specific configuration but lacks the adaptability to evaluate alternative chemistries without substantial modification [27].

This specificity restricts the model's applicability, limiting its utility for broader design efforts, especially as the field of SSBs continues to explore diverse material combinations to address challenges in performance and scalability [29].

In contrast, the SolidPAC toolkit by Dixit et al., which is based on Knehr et al.'s BatPaC for LIBs, represents a departure from these physics-based, detailed interaction models [12,21]. It provides a user-driven, preliminary design model specifically for SSBs, designed to allow user customisation of input parameters and configurations to estimate performance metrics in a more generalised manner. Rather than focusing on intricate physics-based behaviours, the model enables broad performance estimations based on customisable design parameters, thus supporting early-stage design flexibility over detailed simulation accuracy.

SolidPAC offers notable manageability through its intuitive graphical user interface (GUI), which facilitates straightforward navigation and parameter configuration. However, limitations in its clarity and functionality require consideration. The inclusion of numerous input parameters on a single interface, combined with the absence of result visualisation, may introduce ambiguity and complicate the design process. Additionally, issues with reusability and consistency have been observed, particularly in the Python implementation (Version 1), where errors can prevent result generation even with accurate configurations. Although such issues are absent in the Excel version, their presence in the Python version (Version 1) underscores areas for potential improvement.

The toolkit is praiseworthy for its flexibility in enabling macro-scale design, allowing users to customise key parameters such as material selection, electrode thickness, and cell configuration. However, its capacity for iterative design optimisation is limited by the absence of an integrated sensitivity analysis (SA) feature. This shortfall requires users to conduct SA manually, reducing the efficiency of exploring and optimising parameter variations. Furthermore, SolidPAC lacks mechanisms to validate electrochemical material compatibility, leaving this critical responsibility to the user. These limitations hinder the toolkit's effectiveness as a comprehensive design framework, particularly for researchers and developers seeking systematic refinement and validation of battery designs.

To bridge this gap, an integrated approach to SSB design is essential. This article presents a modelling framework developed to support informed decision-making in SSB design and configuration. The model allows users to specify materials and cell configurations, with calculations extending from individual cell components to complete pack configurations. Through user-defined parameters, the model performs key calculations for performance metrics such as energy density, power, and resistance. Additionally, a material compatibility check ensures appropriate selection of anode, cathode, and electrolyte materials, supported by a material database. SA is also incorporated, allowing users to identify critical design parameters affecting KPIs and to optimise configurations accordingly.

The structure of this work is as follows: The modelling section introduces the framework, detailing the design calculations for material and cell levels, and describes key model functionalities, including compatibility checks and SA. The results and discussion section evaluates the model's application to various cell configurations, with a focus on performance metrics and critical design parameters. SA findings are discussed within practical SSB design constraints. Finally, the conclusion summarises the model's contributions and highlights areas for future improvement and research in battery modelling.

2. Methods

The SSB design model introduced in this study provides a systematic framework for the configuration and optimisation of SSBs. The model integrates battery chemistry selection, material compatibility validation, electrochemical calculations, and sensitivity

analysis, enabling users to quantitatively assess KPIs such as energy density, power density, and internal resistance. Implemented in Microsoft Excel and supported by a Visual Basic for Applications (VBA) macro, the model facilitates a user-friendly interface with real-time computation capabilities.

In contrast to existing modelling tools, the present model introduces several distinctive features that address critical methodological gaps. Notably, the model incorporates a material compatibility validation step, which systematically verifies the electrochemical feasibility of selected anode, cathode, and solid electrolyte combinations. Furthermore, while existing modelling tools provide performance estimations for predefined configurations, they do not support integrated sensitivity analysis. The model developed in this study includes a dedicated sensitivity analysis function that allows for the systematic exploration of parameter interdependencies, thereby enhancing the robustness and transparency of design decisions. Additionally, the present model is designed to accommodate a wide range of SSB chemistries and cell configurations without being restricted to predefined material sets or architecture types. This flexibility enhances its applicability as a research tool in the early stages of battery development. Figure 2 provides a visual overview of the computational framework and algorithm, depicted as a flowchart to illustrate the sequential and interconnected phases of the model. It starts with cell design inputs, moves through capacity and dimensional calculations, and concludes with cell design and SA.

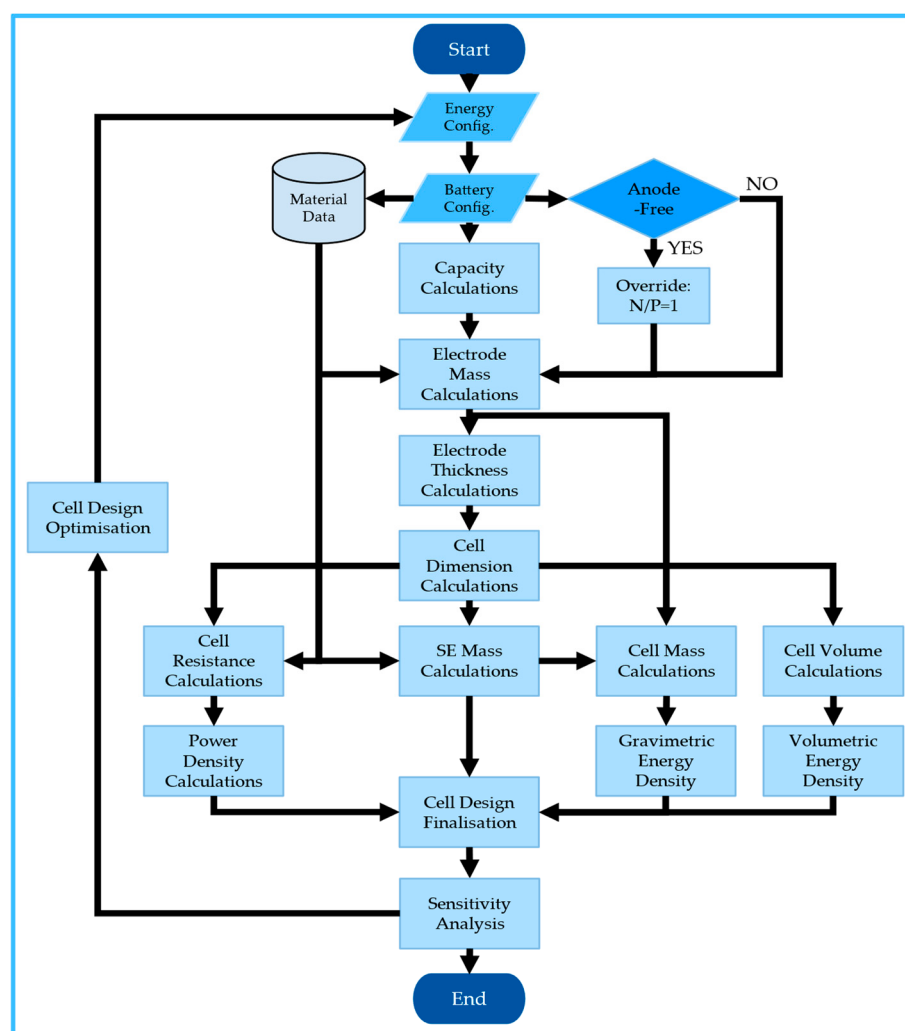


Figure 2. Flowchart of modelling framework for SSB design model.

The model integrates methodologies from SolidPAC and BatPAC, combining the parameter-driven approach of SolidPAC for SSBs with the usability and adaptability of the Excel-based BatPAC model. This hybridisation enables robust performance predictions across diverse SSB configurations while supporting user-driven design flexibility. Core equations for cell and battery dimensioning, such as those for capacity, energy densities, and component dimensions, are adapted from BatPAC [21]. In parallel, the model incorporates linear equations and methodologies from SolidPAC that address the specific properties and challenges of SSBs. These include equations for solid electrolyte resistances, interfacial resistances, and thickness dependencies, which are crucial for accurately modelling SSB behaviour [12]. This hybrid approach bridges the gap between the specific equations of SolidPAC and the broader adaptability of BatPAC, ensuring the model is not restricted to pre-defined chemistries or configurations. As a result, users can explore and optimise a wide range of SSB designs with enhanced usability and adaptability.

2.1. Model User Initiation

The framework begins with the cell design phase, where users input essential parameters, including the target energy capacity, battery chemistry, and cell dimensions. This phase also defines the electrode architecture, encompassing cathode and anode materials, electrolyte composition, and stacking configurations. These inputs form the foundational specifications for the battery. The model features a material database with properties such as theoretical capacities, ionic conductivities, and interfacial resistances for cathode, anode, and electrolyte materials. These data, sourced from experimental research, is provided in Appendix A, Tables A1–A3. The database is not intended to be exhaustive and can be expanded or supplemented by users as needed. If the user opts for an anode-free design, the model automatically sets the negative-to-positive-electrode capacity ratio (N/P ratio) to 1, assuming the anode forms in situ during the formation process [35].

A key feature of the model is its material compatibility validation. Once users specify the battery chemistry, the model cross-references these choices against compatibility data within the database. This step identifies whether the selected materials, such as cathode–electrolyte and anode–electrolyte pairs, are electrochemically compatible. For combinations with limited data, the model flags the issue and notifies the user, ensuring that design decisions are informed and supported by available experimental evidence. These data are also included in Appendix B, Tables A4 and A5.

2.2. Model Cell Configuration

Following material validation, the computational analysis phase calculates key battery parameters, beginning with the pack energy E_{BP} (kWh), which is specified by the user as a design input. This value serves as the basis for determining the battery's capacity and related parameters. It should be noted that the model does not account for capacity degradation mechanisms, such as active material (AM) degradation or the formation of the solid electrolyte interphase (SEI). AM degradation reduces the number of sites available for lithium-ion intercalation, while SEI formation irreversibly consumes lithium ions, leading to a passivation layer on electrode surfaces. These mechanisms, along with other side reactions and self-discharge effects, diminish battery capacity over time but are beyond the scope of the current modelling framework [36]. The pack capacity C_{Pack} (Ah) is calculated using the equation:

$$C_{Pack} = \frac{E_{BP}}{V_{OCV}}, \quad (1)$$

where V_{OCV} (V) is the nominal voltage of the battery pack. This voltage is approximated as the average open-circuit voltage (OCV) across the state-of-charge range, obtained from the material database for the selected cathode and anode combination. By incorporating OCV

data into the calculation, the model ensures realistic capacity predictions tailored to the chosen cell chemistry, simplifying the OCV–state-of-charge (SOC) relationship to a single representative value suitable for system-level modelling, comparisons, or analytical approximations. However, this simplification neglects nonlinearities in the OCV–SOC curve, potentially reducing accuracy for applications requiring detailed voltage dynamics [37].

Once the pack capacity is determined, the model calculates the capacities at the module and cell levels. These calculations incorporate user-defined configurations, specifically the number of cells in parallel and series within a module $N_{Module,parallel}$ and the number of modules in parallel and series within the pack $N_{Cell,parallel}$. The cell-level capacity is given by:

$$C_{Cell} = \frac{C_{Pack}}{N_{Module,parallel} \cdot N_{Cell,parallel}}. \quad (2)$$

Building on the cell-level capacity C_{Cell} (Ah), the model calculates the electrode masses and thicknesses to establish the cell's dimensions. The active material densities used for this calculation are based on literature-reported tapped or bulk densities under standard laboratory conditions. It is acknowledged that these values can vary significantly depending on the applied pressure and compaction method during electrode fabrication, such as uniaxial or isostatic pressing. Variations in pressure conditions can influence the microstructural arrangement of the active material and, consequently, its effective density, which in turn affects both the calculated electrode thickness and the volumetric energy density of the cell [38,39]. While the model does not currently account for the manufacturing of electrode materials under varying pressure regimes, it allows the user to manually adjust the input density values to reflect processing-specific parameters. This flexibility enables the consideration of pressure-dependent effects in a controlled manner, insofar as accurate density data are available for the respective compaction techniques. However, the model does not incorporate a constitutive relationship between applied pressure and resulting density, as this would require a dedicated electro-chemo-mechanical coupling beyond the scope of the present framework.

The cathode active material (CAM) mass is calculated based on its specific capacity, with adjustments made to account for formation losses. This ensures the target capacity is met, compensating for the 10% capacity loss incurred during the formation step in the cell finishing stage of SSB manufacturing. This value is deliberately conservative, serving as a cautious basis for the model's KPI calculations [40]. However, this value is user adjustable. However, this step may become unnecessary with future developments in SSB technology, allowing it to be omitted in the model [41]. The CAM mass is calculated by dividing the adjusted cell capacity, after accounting for formation losses, by the theoretical specific capacity of the CAM material.

After determining the CAM mass, the total cathode mass is calculated by considering the CAM's mass fraction within the cathode composite. This step accounts for the proportions of other components, including the catholyte, carbon conductive additive, and binder, whose masses are determined based on their respective mass fractions. The cathode thickness $t_{Cathode}$ (μm) is calculated using the cathode mass $m_{Cathode}$ (g), the cathode composite density $\rho_{Cathode}$ (g/cm^3), the porosity $\varepsilon_{Cathode}$ (vol%), and the CAM's areal loading λ_{CAM} (mAh/cm^2). The relationship is defined as:

$$t_{Cathode} = \frac{m_{Cathode}}{\rho_{Cathode}} \cdot \frac{100}{100 - \varepsilon_{Cathode}} \cdot \frac{\lambda_{CAM}}{m_{CAM} \cdot c_{CAM}}. \quad (3)$$

The cathode parameters are used to derive the anode design specifications, starting with the N/P thickness ratio. This ratio, determined by the user-defined N/P ratio, depends on the capacity densities of the CAM and the anode active material (AAM), calculated as

the specific capacities divided by material densities. For an anode-free configuration, the N/P thickness ratio is set to zero. The anode thickness is then calculated as the product of the N/P thickness ratio and the cathode thickness.

The next step is to compute the anode mass m_{Anode} (g) based on the cell's formation capacity $C_{Cell,Formation}$ (Ah), the specific capacity of the AAM c_{AAM} (mAh/g), the N/P ratio NP , and the N/P thickness ratio $NP_{Thickness}$. The anode mass is calculated as:

$$m_{Anode} = \frac{C_{Cell,Formation}}{c_{AAM}} \cdot (NP - 1) \cdot \left(1 + \frac{NP_{Thickness}}{100} \right). \quad (4)$$

After determining the electrode mass and thickness, the overall cell dimensions, including width, length, and the number of layers in a stack, are calculated. The stacking architecture, specified by the user, plays a critical role in determining the total number of cell layers N_{Layers} . For bipolar stacking, this is given by:

$$N_{Layers} = \frac{(t_{Cell,Target} - 2 \cdot t_{Casing} - t_{CC,Anode}) \cdot PD}{t_{CC,Anode} + t_{Anode} + t_{Cathode} + t_{Separator}}, \quad (5)$$

where $t_{Cell,Target}$ (mm) is the user-defined target cell thickness, t_{Casing} (mm) is the casing thickness, $t_{CC,Anode}$ is the anode current collector (CC) thickness (μm), and PD is the packing density (%), accounting for voids. The thicknesses of the cathode, anode, separator, and cell stack casing are denoted by $t_{Cathode}$, t_{Anode} , $t_{Separator}$, and t_{Casing} (μm), respectively.

For conventional stacking, the cathode CC thickness $t_{CC,Cathode}$ is included in the equation as follows:

$$N_{Layers} = \frac{(t_{Cell,Target} - 2 \cdot t_{Casing}) \cdot PD}{t_{CC,Anode} + t_{CC,Cathode} + t_{Anode} + t_{Cathode} + 2 \cdot t_{Separator}}. \quad (6)$$

The model rounds the calculated cell layers down to the nearest whole number, as the layers represent discrete physical entities.

After determining the electrode mass and thickness, the overall cell dimensions—including width, length, and volume—are calculated, as shown in Figure 3b,c. These calculations use the cathode dimensions as the reference, with its dimensions derived from the number of cell layers and the surface area required to achieve the target capacity. The width of the cathode $W_{Cathode}$ (mm) is calculated using the following equation:

$$W_{Cathode} = \sqrt{\frac{A_{Cathode \text{ by Total Loading}}}{N_{Layers} \cdot 2 \cdot L / W_{Cathode}}}. \quad (7)$$

The area of the cathode by loading $A_{Cathode \text{ by Total Loading}}$ (cm^2) represents the total surface area of all the cathode layers needed to achieve the desired capacity. It is calculated by dividing the cathode active material mass by its areal loading and specific capacity. The length-to-width ratio $L / W_{Cathode}$ is a user-defined parameter that determines the proportional relationship between the length and width of the cathode. The factor of 2 in the equation accounts for the bilayer coating of the CC, where both sides are coated with material, doubling the surface area for cathode loading. Users can adjust this parameter in the model; for single-layer coatings, the factor of 2 is removed, and calculations are adjusted accordingly to reflect the reduced coating area. Once the cathode width is established, the length $L_{Cathode}$ (mm) is determined as the product of the length-to-width ratio. The remaining cell dimensions are then determined based on the cathode dimensions.

To ensure complete coverage of the cathode and optimise material utilisation during cycling, the anode dimensions include user-defined excess width and length. Similarly,

the separator dimensions are extended beyond those of both the cathode and the anode, incorporating safety margins to prevent short circuits and ensure reliable operation.

The CC dimensions are designed to extend beyond the electrodes, providing space for electrical connections and structural support, thereby improving assembly reliability and overall cell integrity. Terminal dimensions are optimised to balance electrical conductivity and material efficiency, as defined by user-specified parameters and illustrated in Figure 3d. Finally, the complete cell dimensions, including the casing and folded edges, are calculated to encapsulate all components while providing the necessary structural support.

These calculations define the cell's width, length, thickness, and volume, ensuring alignment with the target design specifications. These are adjusted following the approach outlined in BatPAC [21]. Figure 3 illustrates the dimensional hierarchy and proportional layout of the cell components.

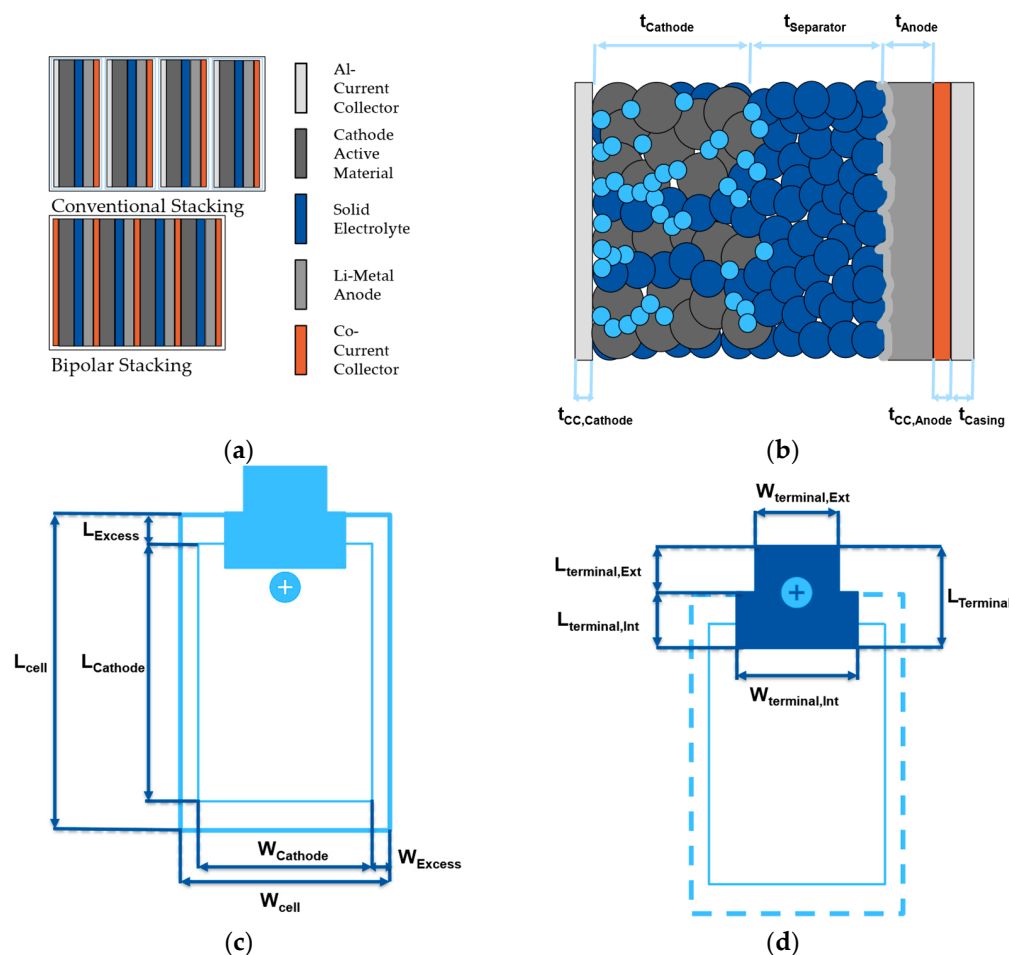


Figure 3. Cell dimension illustrations. (a) Conventional and bipolar cell stacking. (b) Cross-sectional view of the cell stack, illustrating the layered structure of the cathode, separator, anode, and current collectors, along with their respective thicknesses. (c) Layout of the cell's planar dimensions, detailing the width and length relationships between the cathode, anode, separator, and cell casing. (d) Top view of the terminal connections, showcasing the internal and external terminal dimensions and their placement relative to the cell's overall design.

The framework calculates the mass of the SE separator by incorporating the separator thickness, material density, and dimensions. The separator dimensions, including width and length, are oversized relative to the cathode to accommodate volumetric changes during cycling and maintain structural integrity while preventing short circuits. The

separator mass is determined based on the number of cell layers, ensuring alignment with the overall cell architecture.

After completing the separator calculations, the total cell mass is calculated by summing the masses of all components, including the electrodes, separator, CCs, cell casing, and terminals. The cell casing mass is derived using its thickness and density, and the calculated cell width and length. The CC mass is determined separately for the anode and cathode, considering their material properties and stacking configurations. For bipolar stacking, only the anode CC is included, as the cathode CC is replaced by a shared bipolar current collector. In contrast, conventional stacking includes both anode and cathode CCs.

Terminal masses are calculated based on their internal and external dimensions, as well as their material properties. Bipolar configurations use copper for both terminals, whereas conventional configurations employ copper for the anode and aluminium for the cathode. These masses are scaled according to the stacking architecture to ensure the design meets the required electrical and structural performance.

2.3. Model Key Performance Indicator Computations

The energy density calculations begin by deriving cell energy while accounting for capacity losses due to electrical resistance. This involves calculating the voltage drop caused by electrical resistance, which, similar to BatPAC, incorporates the area-specific impedance of the cathode material, cell capacity, C-rate (set to C/3), and cathode dimensions. The nominal voltage V_N (V) is subsequently determined by subtracting the calculated voltage drop from the average cell voltage. Cell energy is then calculated based on the nominal voltage, as shown in Equation (1).

Then, the gravimetric energy density E_{Grav} (Wh/kg) and volumetric energy density E_{Vol} (Wh/L) are calculated by dividing the adjusted cell energy by the total cell mass m_{Cell} (kg) and volume v_{Cell} (L), respectively. These relationships are expressed as:

$$E_{Grav} = \frac{E_{Cell}}{m_{Cell}}, \quad (8)$$

$$\text{and } E_{Vol} = \frac{E_{Cell}}{v_{Cell}}. \quad (9)$$

The model accounts for the mass and volume of the cell's casing, connectors, and other immediate components but excludes ancillary components at the battery module and pack levels, such as cooling systems, structural supports, and wiring.

The calculation of the internal resistance of the cell R_{Cell} (Ω), which depends on the stacking configuration, incorporates the resistances of the anode, cathode, separator, CCs, and terminals. The modelling framework adopts several simplifying assumptions for these calculations. The effects of temperature on ionic conductivity, interfacial resistance, and state-of-charge dependence are omitted, resulting in resistance values that remain constant under varying operating conditions [42]. This simplification affects the accuracy of the model when applied to SSB designs based on polymer SE, which typically require elevated operating temperatures to achieve sufficient ionic conductivity [43]. Consequently, such designs may not reflect their full performance potential within the current modelling framework. However, the model allows users to manually adjust material properties in the material data to approximate specific operating conditions. Additionally, material properties are assumed to remain static, with no variations in parameters such as degradation or state of charge throughout operation.

The anode and cathode resistances R_{Anode} (Ω) and $R_{Cathode}$ (Ω) are calculated by dividing the interfacial resistance of their respective material interfaces by the surface area. These relationships are expressed as:

$$R_{Anode} = \frac{r_{Int, AAM/SE}}{W_{Anode} \cdot L_{Anode}}, \quad (10)$$

$$\text{and } R_{Cathode} = \frac{r_{Int, CAM/SE}}{W_{Cathode} \cdot L_{Cathode}}. \quad (11)$$

Here, $r_{Int,AAM|SE}$ ($\Omega \text{ cm}^2$) and $r_{Int,CAM|SE}$ ($\Omega \text{ cm}^2$) are the interfacial resistances at the AAM|SE and CAM|SE interfaces, respectively. These quantify the impedance to ionic charge transfer at the solid–solid interfaces between the anode or cathode active material and the solid electrolyte. They are key contributors to the total cell resistance and to power limitations in solid-state batteries. These resistances are typically measured experimentally using electrochemical impedance spectroscopy (EIS), often in symmetric or full-cell configurations [44,45].

The separator resistance $R_{Separator}$ (Ω) accounts for ionic conductivity and is influenced by the separator’s thickness, dimensions, and ionic conductivity $\sigma_{Separator}$ (mS/cm). A uniform ionic conductivity is assumed across the separator, disregarding potential gradients or defects that could result from mechanical stress or thermal effects [42]. It is calculated as:

$$R_{Separator} = \frac{t_{Separator}}{\sigma_{Separator} \cdot (W_{Separator} \cdot L_{Separator})}. \quad (12)$$

Once the internal resistance is established, the cell power is calculated using Ohm’s law. The cell current I_{Cell} (A), which is influenced by stacking configuration, is determined by dividing the nominal voltage and by the total cell resistance:

$$I_{Cell} = \frac{V_N}{R_{Cell}}. \quad (13)$$

The total cell power P_{Cell} (W) is then obtained by multiplying the nominal voltage and cell current:

$$P_{Cell} = V_N \cdot N_{Layers} \cdot I_{Cell}. \quad (14)$$

Finally, the gravimetric P_{Grav} (W/kg) and volumetric P_{Vol} (W/kg) power densities are calculated as:

$$P_{Grav} = \frac{P_{Cell}}{m_{Cell}}, \quad (15)$$

$$\text{and } P_{Vol} = \frac{P_{Cell}}{v_{Cell}}. \quad (16)$$

2.4. Model Sensitivity Analysis Function

The SA and design optimisation methodology uses a VBA macro integrated within Excel to iteratively adjust key design parameters and evaluate their effects on performance metrics. The process employs a local SA method, known as one at a time (OAT), where parameters such as the N/P ratio, cathode loading, and electrolyte thickness are varied individually while others remain constant. This approach isolates the influence of each parameter on KPIs such as gravimetric energy density, volumetric energy density, cell power, and cell resistance. Target values for each KPI are determined using the equation:

$$KPI_{Target} = KPI_{Baseline} \left(1 \pm \frac{Improvement\ Target}{100} \right), \quad (17)$$

where $KPI_{Baseline}$ represents the initial design values, and the user-defined improvement percentage sets the adjustment goals for optimisation. The VBA macro iteratively adjusts parameters based on a proportional adjustment factor (Supplementary Information) until either the target value is achieved, or the parameter reaches predefined boundaries. These boundaries ensure manufacturability and feasibility, balancing optimisation with practical constraints.

To measure the sensitivity of KPIs to changes in design parameters, the sensitivity factor $SF_{Parameter}$ is calculated as:

$$SF_{Parameter} = \frac{(KPI_{Adjusted} - KPI_{Baseline}) / KPI_{Baseline}}{(Parameter_{Adjusted} - Parameter_{Baseline}) / Parameter_{Baseline}}. \quad (18)$$

This factor captures the relative impact of parameter variations on KPI outcomes, highlighting the most influential design variables for optimisation.

2.5. Model Cell Configuration Finalisation

The final stage of the model framework consolidates all calculations to generate comprehensive design specifications. Component masses and dimensions are compiled, and graphical representations, such as tree maps for mass distribution and bar charts for dimensions, provide insights into the cell's spatial layout. KPIs, including energy and power density and internal resistance, are presented to evaluate design efficiency and performance.

The user can assess whether the architectural configuration meets the desired performance targets before proceeding to development or production. The SA results are displayed in a column chart, highlighting the impact of parameter variations on KPIs. Based on this analysis, the user may optimise the design by adjusting parameters. Any adjustments restart the modelling framework (Figure 2), updating all calculations and evaluations accordingly.

3. Results

This section systematically evaluates the model's performance and applicability, divided into two sections: Validation of Model Accuracy and Validation of Model Application for Design and Development. Each section addresses distinct objectives to demonstrate the robustness and utility of the modelling framework and toolkit.

3.1. Validation of Model Accuracy

The first section, Validation of Model Accuracy, assesses the model's predictive reliability by benchmarking its outputs against experimental data. The selected experimental data correspond to cell configurations closely aligned with anticipated specifications for commercial designs, particularly in terms of electrode and electrolyte thickness and dimensions, which are key limiting factors in experimental cell designs [11]. This ensures realistic comparisons and underscores the model's relevance for future applications in battery design and development. Experimental cells are replicated within the model with the highest possible accuracy. However, full replication was occasionally limited by insufficient information and data [46]. Any missing data are explicitly noted to maintain transparency and to identify areas where additional experimental characterisation would be valuable. A systematic comparison of experimental and model-generated KPIs provides a quantitative measure of the model's accuracy in predicting real-world battery performance. An overview of the selected experimental designs is provided in Table 2.

Table 2. Experimental cell designs for model accuracy validation.

Ref.	Cell Chemistry	Gravimetric Energy Density [Wh/kg]	Volumetric Energy Density [Wh/L]	Gravimetric Power Density [W/kg]
Dixit (2022) [12]	Li LLZO NMC622	298.06	1692.43	-
Tan (2021) [47]	Si LiPSCl NCM811	-	974	-
Nam (2018) [48]	Graphite LiPSCl NCM622	184	432	-

Adjusting values not specified in experimental designs is essential to aligning the model's outputs with the KPIs of experimental results. For instances where energy capacity is not explicitly stated, it is assumed to fall within a typical range of 0.005 Wh to 5 Wh for laboratory-scale single-layer cells [49]. Within this range, the input value is manually adjusted in the model to match the experimental KPIs.

The N/P ratio is another parameter rarely reported in experimental data but has a significant impact on the anode's excess thickness [50,51]. To approximate the reported anode thickness in experimental designs, the ratio is adjusted within the model accordingly. Experimental cells often utilise single-layer or alternative layering configurations [52,53]. This parameter cannot be directly adjusted in the model. However, this can be approximated by reducing the target cell thickness until a single-layer design is achieved. Finally, the calculation of KPIs, such as gravimetric and volumetric energy and power densities, presents challenges when experimental values are unavailable or derived using unspecified methodologies. Experimental studies frequently omit contributions from casing and terminal materials in their KPIs, considering only the weights of electrodes, electrolytes, and current collectors. To ensure consistency, the model's KPI calculations are manually adjusted to exclude these components during comparisons with experimental results. This approach ensures the comparison remains accurate despite methodological differences in reporting.

When specific values are absent in the experimental designs, standard parameters are applied and kept constant throughout the modelling process. These parameters primarily include cell dimensions, such as those of the CCs, terminals, and casing, and the use of a conventional stacking configuration. Derived from the default settings of the BatPAC pouch cell modelling framework, these values ensure consistency across the comparisons [21]. Additionally, for electrochemical parameters, the cell's capacity loss after the formation process is standardised at 10%.

The validation of the model's accuracy involves a comparative analysis with results from the SolidPAC framework developed by Dixit et al. [12]. Although not a direct comparison with experimental data, this analysis leverages the SolidPAC model, which has been extensively validated against experimental results. Using such a well-established benchmark strengthens the credibility of the comparative analysis and enables the assessment of the developed framework's accuracy and robustness.

To ensure comparability, the same cell chemistry (Li | LLZO | NMC622) and equivalent values for cell configuration and dimensions were applied wherever possible, as detailed in Table A4. However, slight deviations from the original configuration were observed in cell dimensions and cell mass. The comparison focuses on KPIs, including gravimetric energy density, volumetric energy density, and gravimetric power density. However, as the current version of SolidPAC does not calculate gravimetric power density, this metric cannot be compared. The results, summarised in Table 3, highlight variances in KPI values between the two models.

Table 3. Dixit et al.'s [12] cell designs.

Cell Chemistry	Ref.	Gravimetric Energy Density [Wh/kg]	Volumetric Energy Density [Wh/L]	Gravimetric Power Density [W/kg]
Li LLZO NMC622	Dixit (2022) [12]	298.06	1692.43	-
	Model Results	263.72	1699.04	538.44
Accuracy		-11.52%	+0.39%	n/a

For gravimetric energy density, the model predicted 263.72 Wh/kg, a -11.52% variance compared to SolidPAC's 298.06 Wh/kg. In contrast, the model estimated a volumetric energy density of 1699.04 Wh/L, representing a +0.39% variance from SolidPAC's 1692.43 Wh/L. These differences stem from variations in methodology and equations, particularly in the calculation of nominal voltage and cell mass.

The model's accuracy was further evaluated by comparing its predictions to the experimental design reported by Tan et al. (2021) [47]. This comparison focused on the cell chemistry (Si | LiPSCl | NCM811). The model's compatibility validation function identified that NCM811 and LPSCl materials are not electrochemically compatible. To address this issue, the experimental design incorporated a coating on the cathode to mitigate compatibility challenges. However, this coating, which affects electrochemical performance, is not accounted for in the model and may contribute to minor discrepancies in performance predictions.

This comparison is reliable due to the detailed documentation of the experimental design, enabling the model to closely replicate the cell configuration and dimensions using the parameters in Table A5. For modelling, the target energy was set to 11.64 Wh to match the experimentally reported cell capacity of 3 Ah. However, deviations were observed between the reported and model-calculated thicknesses of the anode and cathode. The model-calculated anode thickness was 10.11 μm , representing a -25.1% deviation from the reported value of 13.5 μm . Similarly, the model-calculated cathode thickness was 139.87 μm , corresponding to a +16.6% deviation from the reported value of 120 μm .

The comparison specifically focuses on volumetric energy density, the only KPI disclosed by Tan et al. [47]. The results, detailed in Table 4, reveal differences in KPI values between the two designs.

Table 4. Tan et al.'s [47] cell designs.

Cell Chemistry	Ref.	Gravimetric Energy Density [Wh/kg]	Volumetric Energy Density [Wh/L]	Gravimetric Power Density [W/kg]
Si LiPSCl NCM811	Tan (2021) [47]	-	974	-
	Model Results	364.44	975.90	938.43
Accuracy		n/a	+0.19%	n/a

The experimental design reported a volumetric energy density of 974 Wh/L, while the model predicted 975.90 Wh/L, reflecting a +0.19% accuracy. This precision highlights the model's robustness in replicating experimental conditions. The minimal variance in volumetric energy density indicates that the model effectively captures the cell's overall performance. However, the difference in volume suggests that the modelled cell achieves a higher energy content than the experimental cell. Since the energy content of the experimental design is not provided, this cannot be directly confirmed. The discrepancies likely arise from differences in nominal voltage and the specific capacity of the materials, as the model relies on theoretical values for these parameters.

The model was additionally validated by comparing its outputs to experimental data reported by Nam et al. [48]. This analysis focused on a single-layer cell with the chemistry Graphite | LiPSCl | NCM622. It is important to highlight that the model flagged a warning regarding the electrochemical material incompatibility between the cathode and the electrolyte. Nam et al. [48] mitigated this issue experimentally by coating the cathode, a feature that cannot currently be simulated within the model framework.

The target energy of the cell was estimated at 0.394 Wh, a value not explicitly reported by Nam et al. [48]. This estimation was based on the provided volumetric energy density and an approximation of the active component volumes. However, this approximation resulted in a capacity of only 111 mAh, falling short of the reported 405 mAh. Additionally, the N/P ratio and cathode loading were adjusted to match the reported anode and cathode thicknesses, respectively. Furthermore, the anode CC material was changed to nickel. Through these parameter adjustments, the reported dimensions of the electrodes and solid electrolyte were closely replicated, with deviations kept below 0.5%.

The results of the comparison are summarised in Table 5, which presents the calculated gravimetric and volumetric energy densities. The model predicted a gravimetric energy density of 190.37 Wh/kg, compared to Nam et al.'s [48] reported value of 184 Wh/kg, resulting in a variance of +3.46%. Similarly, the model estimated a volumetric energy density of 476.61 Wh/L, compared to Nam et al.'s [48] 432 Wh/L, with a variance of +3.96%. These calculations were adjusted to match Nam et al.'s [48] methodology, which considered only the active components—electrodes, separator, and CCs—when calculating weight. Yet, the method used to calculate the volume for determining the volumetric energy density is not clearly specified. If the energy densities were instead based on full pouch cell parameters, including casing and terminal materials, the KPIs would be significantly lower due to the additional weight and volume of these components.

Table 5. Nam et al.'s [48] cell designs.

Cell Chemistry	Ref.	Gravimetric Energy Density [Wh/kg]	Volumetric Energy Density [Wh/L]	Gravimetric Power Density [W/kg]
Graphite LiPSCl NCM622	Nam (2018) [48]	184	432	8.2 *
	Model results	190.37	476.61	8.21 **
Accuracy		+3.46%	+3.96%	-0.06%

* Value cited from a secondary source [11]. ** Model approximation based on calculated capacity and reported C-rate.

3.2. Validation of Model Application for Design and Development

The following section validates the model's functionality as a comprehensive toolkit for the preliminary stages of battery design and development. This validation involves simulating practical design scenarios by replicating potential design pathways proposed by leading SSB developers. By utilising the model's predictive capabilities and adaptability, these designs are reverse-engineered and evaluated for feasibility based on limited but essential data [54].

To achieve this, the model integrates and analyses fragmented data from diverse sources, including shareholder letters, patents, and academic research articles, which provide partial insights into the design strategies of key industry players. Given the limited availability of explicit data on cell chemistries, the model extrapolates feasible design pathways and simulates multiple configurations for each company, enabling a systematic assessment of potential commercial cell designs.

The results identify the most viable configurations, offering insights into the advancement of SSB technologies. This analysis underscores the model's capability to support

early-stage decision-making in battery development, particularly when comprehensive experimental data are unavailable.

The following section examines the design and modelling of QuantumScape's QSE-5B cell concept, which features an innovative anode-free architecture combined with a ceramic solid electrolyte. This design is compatible with both NCM and LFP cathodes, representing a significant advancement in solid-state battery technology by targeting high energy densities while ensuring versatility with diverse cathode materials [8,55–58]. An overview of the cell's design and configuration is illustrated in Figure 4a–d.

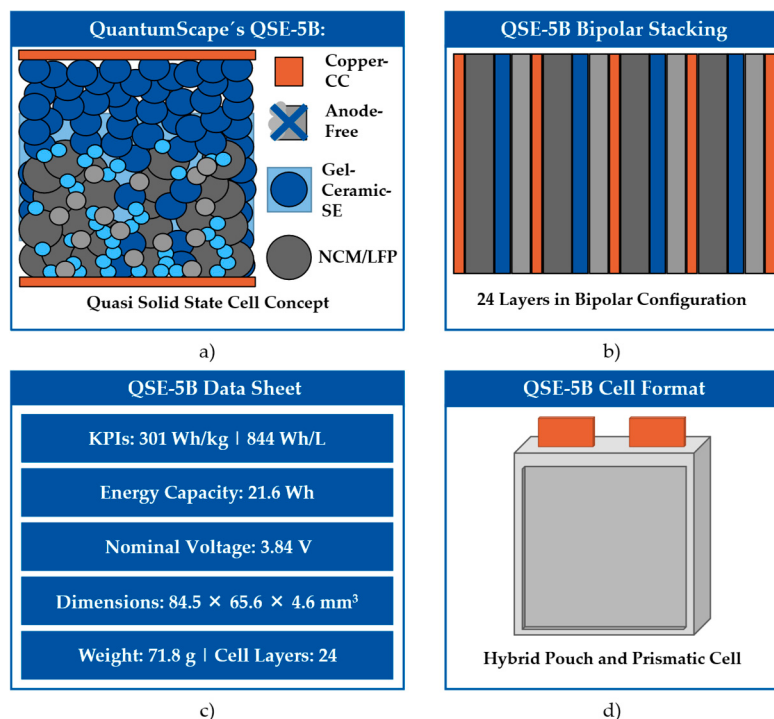


Figure 4. QuantumScape's QSE-5B cell concept. (a) Cell chemistry and concept. (b) Bipolar stacking configuration. (c) Cell data sheet [57,58]. (d) Hybrid pouch and prismatic cell format. The different cell layers are described in Figure 3a.

QuantumScape reports gravimetric and volumetric energy densities of 301 Wh/kg and 844 Wh/L, respectively, for this design, highlighting its potential for commercial application. Publicly available data on the cell's dimensions and configurations have been meticulously compiled from multiple sources and are summarised in Table A7 [57,58]. These parameters provide the basis for the subsequent modelling and analysis of this cell concept.

Using the compiled data and research-supported assumptions, the QSE-5B battery design was reverse-engineered with the developed model. The primary objective was to replicate QuantumScape's reported gravimetric and volumetric energy densities by systematically modelling various configurations. Known parameters, such as cathode loading, target cell energy capacity, and target cell thickness, were directly integrated into the model. Unknown parameters were estimated using literature-based assumptions to align with the known parameters and KPI values. It should be noted that the quasi-solid-state battery with a gel-ceramic catholyte cannot be reproduced using the model. Multiple configurations (QS1–QS3) were tested by varying cathode compositions, catholytes, and cell dimensions. The resulting modelled concepts are summarised in Table 6.

Table 6. QuantumScape’s cell concepts for modelling.

Concept Name	Cell Chemistry	Cathode Composition (CAM, Catholyte, Carbon, Binder) [wt%]	Cathode Porosity [vol%]	Electrolyte Thickness [μm]
QS1	AF LLZO LLZO-NCM622	85:10:2.5:2.5	35	21
QS2	AF LLZO LATP-LFP	91:5:2:2	14	15
QS3	AF LLZO LLTO-NCM811	82:13:2.5:2.5	38	23

The results of the reverse-engineered QSE-5B designs are illustrated in Figure 5, highlighting the QS1, QS2, and QS3 cell concepts. These designs closely replicate the reported dimensions and KPIs of the QSE-5B cell, with minor variations in battery chemistry, cathode composition, electrolyte thickness, and cell dimensions. Each design incorporates an anode-free architecture with a ceramic solid catholyte (e.g., LLZO, LATP, or LLTO) and various cathode compositions, including NCM622, NCM811, and LFP, as shown in Table 6. While alignment with QuantumScape’s reported metrics is high, systematic adjustments to parameters were required to refine the modelled configurations.

Adjustments to cell and cell casing dimensions (length-to-width ratios, cell packing densities) were made to optimise the cell’s performance metrics. These modifications facilitated the systematic exploration of configurations capable of achieving QuantumScape’s reported energy density metrics.

The comparison of KPI metrics and dimensions between the reverse-engineered designs (QS1–QS3) and the QuantumScape QSE-5B benchmark is shown as a heatmap in Figure 6. The design QS3, illustrated in Figure 5c, demonstrates the closest alignment with the QSE-5B benchmark, achieving comparable metrics in gravimetric and volumetric energy densities, nominal voltage, and cell dimensions. While QS1 and QS2 also approximate the benchmark, deviations in certain KPIs and dimensions position QS3 as the most representative configuration.

Based on the provided data from QuantumScape and the modelling framework, it is inferred that the QSE-5B design employs an anode-free architecture combined with a ceramic oxide electrolyte, likely LLZO, with a thickness of approximately 23 μm . The cathode composition is most likely based on NCM811, with a weight ratio of 83:13:2.5:2.5 and a porosity of approximately 38%, allowing the gel component of the catholyte to effectively fill the voids. While LLTO is considered the catholyte material in QS3, LLZO remains a plausible alternative. Furthermore, the QSE-5B design is inferred to utilise a bipolar stacking configuration with single-layer coating of the CCs.

Although the manufacturability of the QS3 design cannot be quantitatively assessed using the model, the defined and modelled parameters fall within the limits of what is currently achievable with existing SSB manufacturing technologies [7,59–64]. Further details on the QS3 design and its configuration are provided in the Supplementary Information.

A further cell concept that can be reverse-engineered employing the model to validate its functionality is ProLogium’s large lithium ceramic battery (LLCB) concept. The information is primarily derived from ProLogium’s press releases and website [65,66]. Despite the limited publicly available information compared to QuantumScape’s QSE-5B, sufficient data on the LLCB cell concept has been compiled to enable reverse-engineering and subsequent analysis.

The LLCB employs a silicon oxide anode paired with an NCM811 catholyte composite. Both the catholyte and solid electrolyte utilise ceramic oxide materials. The LLCB achieves gravimetric and volumetric energy densities of 321 Wh/kg and 749 Wh/L, respectively. While ProLogium has reported more recent optimised designs with improved KPIs, no

detailed data on these improvements are available, restricting the current analysis to the publicly disclosed LLCB concept. Figure 7a–d illustrates the LLCB concept's design and key parameters.

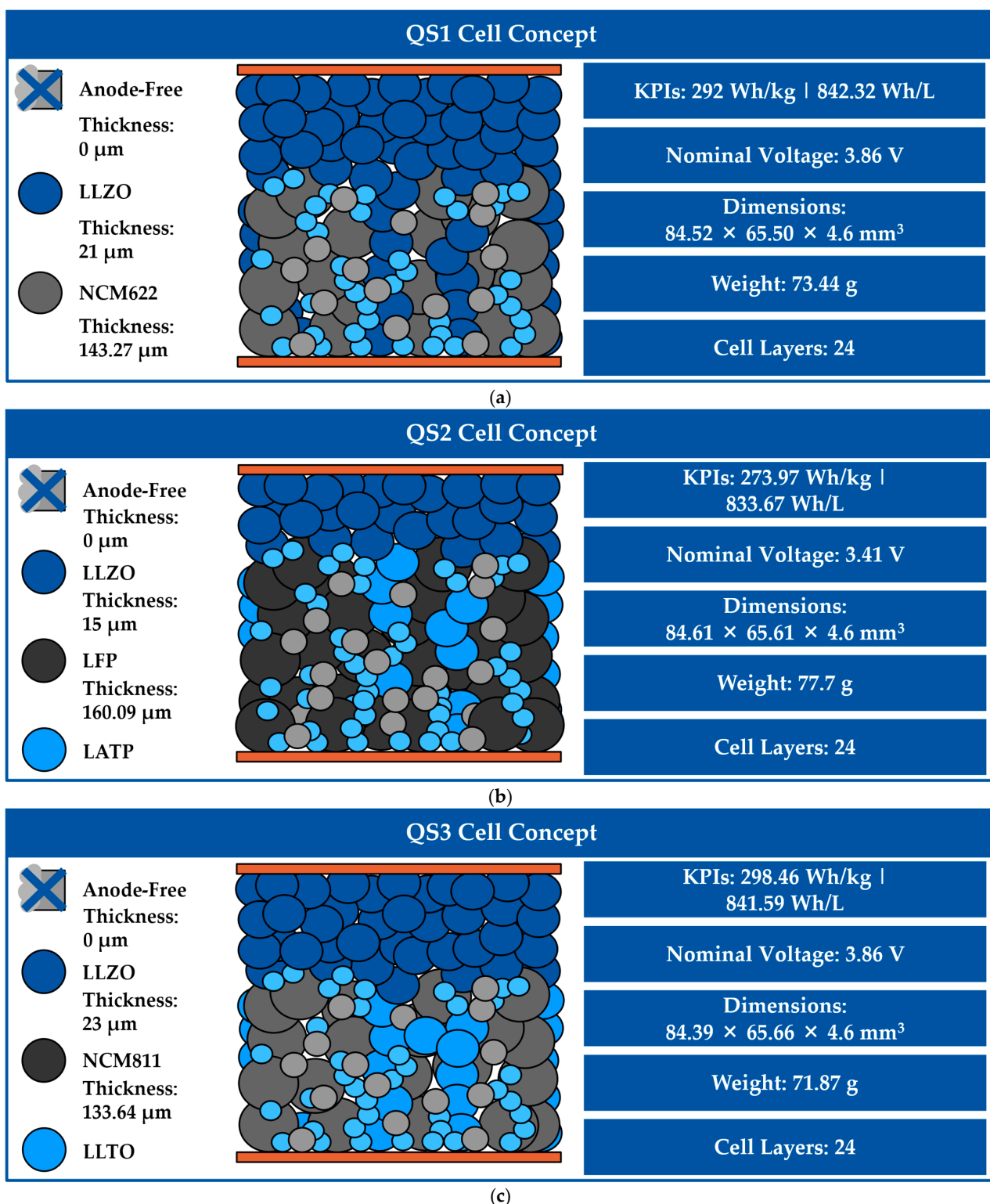


Figure 5. QuantumScape's QSE-5B cell concept reversed-engineered (cell in pristine condition, prior to lithium plating of anode). (a) QS1 cell concept. (b) QS2 cell concept. (c) QS3 cell concept. The different cell layers are described in Figure 3a.

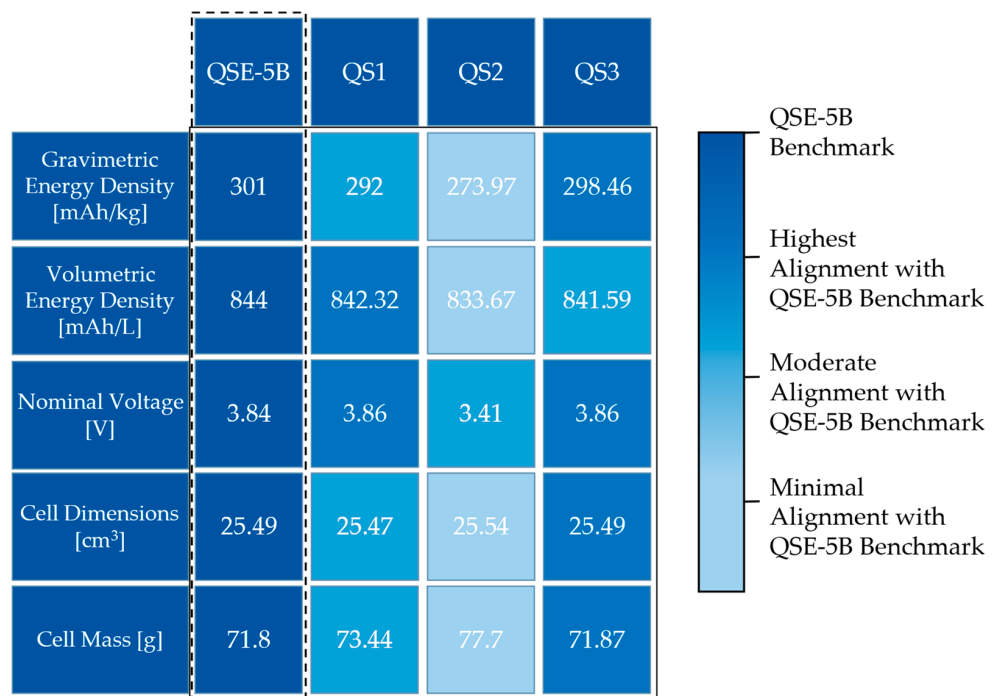


Figure 6. Heatmap comparing reversed-engineered designs (QS1–3) to the QSE-5B benchmark based on dimension and KPI variances. Values framed by the black dashed line represent benchmark values of the QSE-5B cell, as reported by QuantumScape.

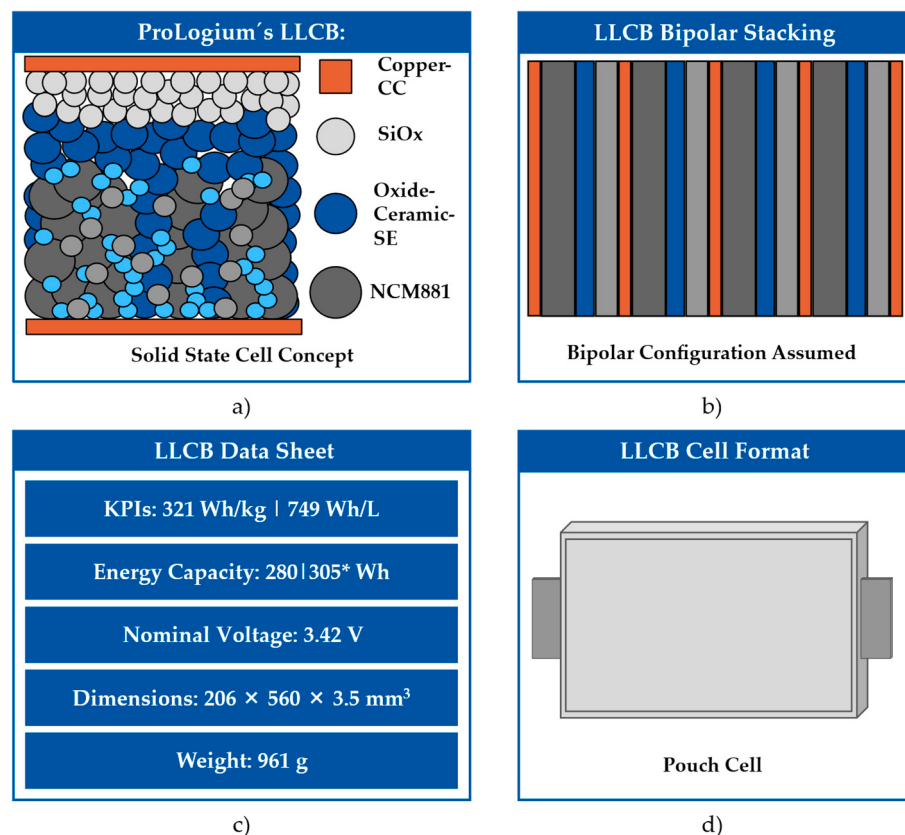


Figure 7. ProLogium's LLCB cell concept. (a) Cell chemistry and concept. (b) Bipolar stacking configuration. (c) Cell data sheet (* energy capacity adjusted for formation loss). (d) Pouch cell form factor. The different cell layers are described in Figure 3a.

With the model, the LLCB design is reverse-engineered to match the KPIs reported by ProLogium. Known parameters, such as target cell energy capacity and cell thickness, are directly incorporated into the model. For parameters not explicitly stated—such as NP ratio, cathode loading, stacking configuration, and the number of cell layers—assumptions are applied to align the simulated results with the reported KPIs. With these assumptions, the model reflects both ProLogium's design principles and practical manufacturing constraints [7]. The modelled configurations, designated as PL1 to PL3, are summarised in Table 7.

Table 7. ProLogium's cell concepts for modelling.

Concept Name	Cell Chemistry	Cathode Composition (CAM, Catholyte, Carbon, Binder) [wt%]	Cathode Porosity [vol%]	Cathode Loading [mAh/cm^2]	NP-Ratio [-]	Electrolyte Thickness [μm]
PL1	SiOx LLZO LLZO-NCM811	86:10:2:2	38	6.5	1.4	24
PL2	SiOx LATP LATP-NCM811	80:15:2.5:2.5	39	6.9	1.7	34
PL3	SiOx LLTO LLTO-NCM811	85:10:2.5:2.5	37	7.4	1.9	26

Due to the limited availability of detailed public data, there is greater design flexibility when modelling the PL1–PL3 cell concepts. This flexibility allows for more significant variations in cell parameters, leading to greater design variance among the modelled configurations. While this enables a broader exploration of potential design pathways, it also introduces variability that must be considered when comparing the PL1–PL3 concepts later.

The results of the reverse-engineered LLCB designs are shown in Figure 8a–c, illustrating the PL1, PL2, and PL3 cell concepts. The active electrode materials remain consistent across the concepts, utilising silicon oxide for the anode and NCM811 for the cathode. However, differences in cathode composition, porosity, and cathode loadings, ranging from 6.5 to 7.4 mAh/cm^2 , result in variations in cathode thickness. Additionally, the N/P ratio, which varies between 1.4 and 1.7, influences the anode thickness in the respective concepts.

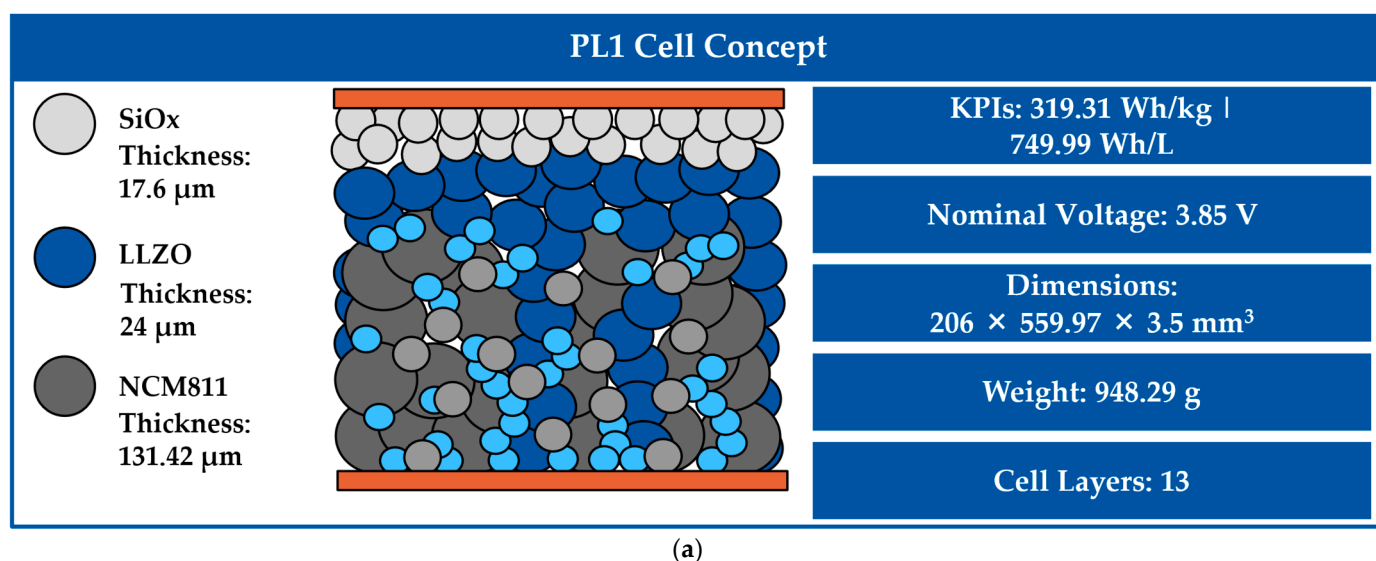


Figure 8. Cont.

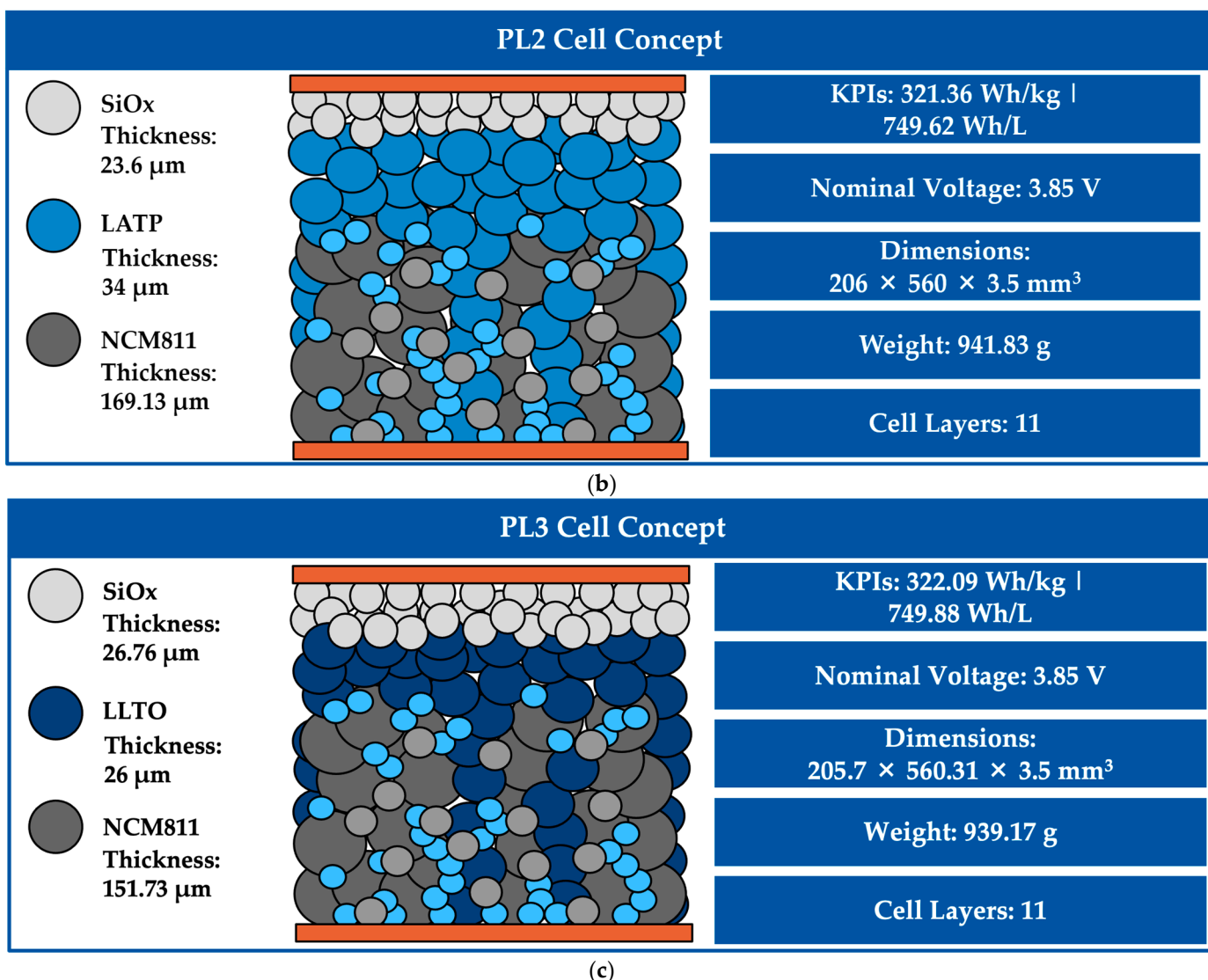


Figure 8. ProLogium’s LLCB cell concept reversed-engineered. (a) PL1 cell concept. (b) PL2 cell concept. (c) PL3 cell concept. The different cell layers are described in Figure 3a.

The selection of ceramic oxides for the electrolytes and catholytes (LLZO, LATP, and LLTO) varies across the designs, and there are significant differences in electrolyte thickness. Notably, PL2 displays an outlier electrolyte thickness compared to that of PL1 and PL3. These variations, combined with ProLogium’s target cell thickness of 3.5 mm, determine the number of bipolar cell layers in each design. Although not explicitly specified by ProLogium, the concepts achieve the energy target with 11 to 13 layers.

Adjustments to cell and casing dimensions, including length-to-width ratios and cell packing densities, were made to optimise the performance metrics of the LLCB designs. Additionally, the terminal material in the model was modified to aluminium for all concepts to align with ProLogium’s design specifications. As in the standardised bipolar stacking configuration, copper serves as the terminal material. Specific adjustments for each configuration are detailed in the Supplementary Information. These modifications enabled a systematic exploration of design pathways to meet ProLogium’s reported metrics.

The comparison of KPI metrics and dimensions between the reverse-engineered designs (PL1–3) and the ProLogium LLCB benchmark is presented as a heatmap in Figure 9. Among the configurations, PL2 emerges as the most representative model of the LLCB design. The PL2 concept aligns closely with the energy densities and cell dimensions, while

the PL1 concept better corresponds to the cell mass. However, all concepts show significant deviations from the reported LLCB mass.

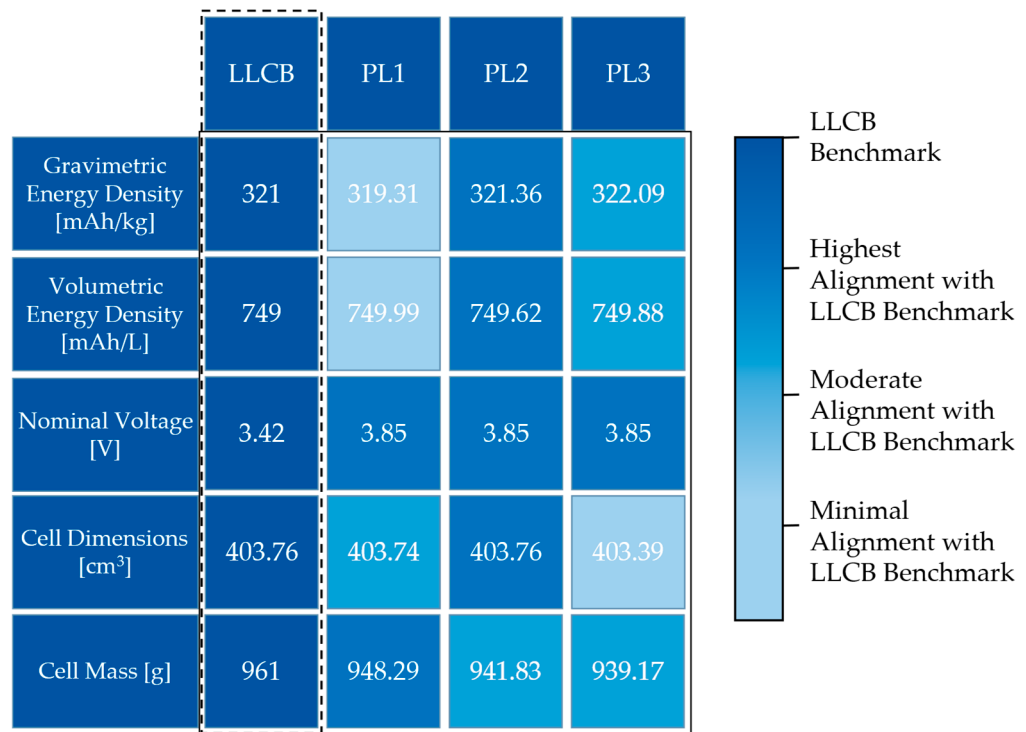


Figure 9. Heatmap comparing reversed-engineered designs (PL1–3) to LLCB benchmark based on dimension and KPI variances. Values framed by the black dashed line represent benchmark values of the LCCB cell, as reported by ProLogium.

According to the data provided by ProLogium and the modelling framework, the LLCB design is believed to utilise a silicon oxide anode paired with a ceramic oxide electrolyte, most likely LATP, with an estimated thickness of 36 µm in the PL2 configuration. The cathode is anticipated to consist of NCM811, with a composition ratio of 80:15:2.5:2.5, a cathode loading of approximately 6.9, and a porosity of approximately 39%, with an N/P ratio of approximately 1.7. While LATP is considered the primary choice for the electrolyte and catholyte in PL2, other ceramic oxides, such as LLZO and LLTO, remain plausible alternatives for the electrolyte and catholyte in ProLogium's system. Additionally, the design is presumed to adopt a bipolar stacking configuration with a single-sided coating on the CCs.

Although a quantitative assessment of the manufacturability of the PL designs, similar to QS, is not possible, the defined and modelled parameters are within the practical limits of current SSB manufacturing techniques [7,59–64,67].

3.3. Application of Sensitivity Analysis in Cell Design Optimisation

The SA function embedded within the modelling framework serves as a tool for evaluating the impact of key design parameters on critical KPIs. By systematically varying specific variables, such as cathode composition, N/P ratio, and electrolyte thickness, the SA quantitatively characterises the relationships between these parameters and the resulting KPIs, as shown in Equations (16) and (17).

The cell optimisation is performed on the QS3 and PL2 cell designs using their baseline concepts and the integrated SA function. While the SA evaluates KPIs such as gravimetric and volumetric energy densities, internal resistance, and power density, the focus is placed on energy densities, as these are the primary metrics reported for these cell concepts.

For the QS3 design, the sensitivity analysis identified cathode loading and electrolyte thickness as the most influential parameters for optimising energy densities. However, the low-sensitivity factors for both gravimetric and volumetric energy densities indicate that significant adjustments are needed to achieve meaningful KPI improvements. This suggests that the QS3 concept is already near its optimal configuration within the constraints of its design parameters. The results of the sensitivity analysis are presented in Figure 10.

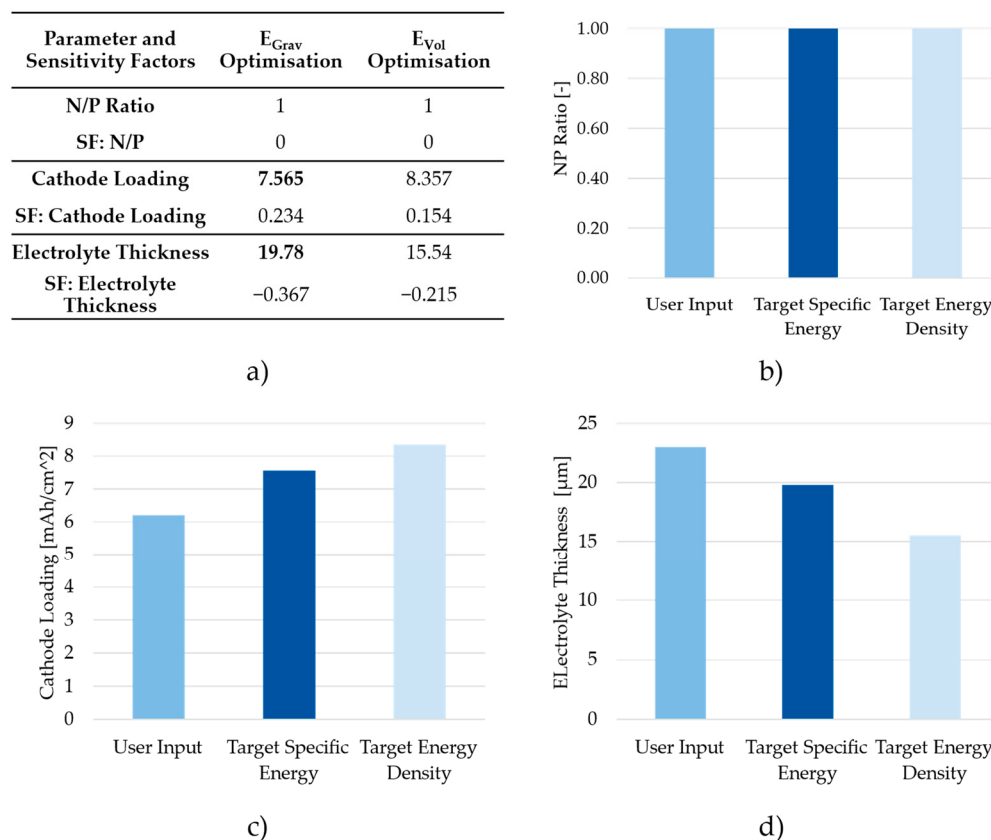


Figure 10. Sensitivity analysis with a 5% KPI improvement target: optimised parameters, sensitivity factors (SFs), and comparative assessments of key design variables. (a) Optimised parameters and their corresponding sensitivity factors (SFs) from the conducted SA. (b) Comparison of the initial and optimised N/P ratio, demonstrating no further improvement potential due to the anode-free design. (c) Comparison of the initial and optimised cathode loading to achieve the 5% improvement target. (d) Comparison of the initial and optimised electrolyte thickness to achieve the 5% improvement target.

Additionally, the N/P ratio, being inherently optimal in the anode-free design, offers no further room for improvement [51,59,68]. Optimisation attempts led to improvements of +12.83% in gravimetric energy density and +5.52% in volumetric energy density. These results underscore the QS3 concept's advanced level of optimisation. The results of the sensitivity analysis and the optimised QS3 cell concept are shown in Figure 11.

For the PL2 design, the SA identified the N/P ratio as the most influential parameters impacting volumetric energy density. The initial SA, targeting a 4% KPI improvement, demonstrated moderate enhancements with minor adjustments to the N/P ratio. To further investigate optimisation potential, a second SA with a 10% improvement target was conducted, uncovering additional opportunities, particularly in cathode loading and electrolyte thickness. The sensitivity analysis results are shown in Figure 12.

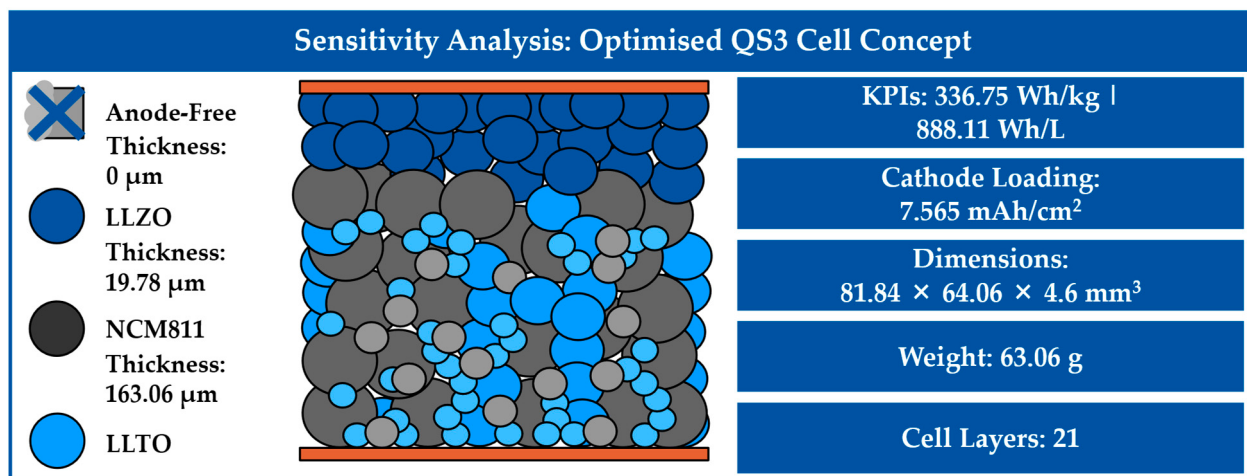
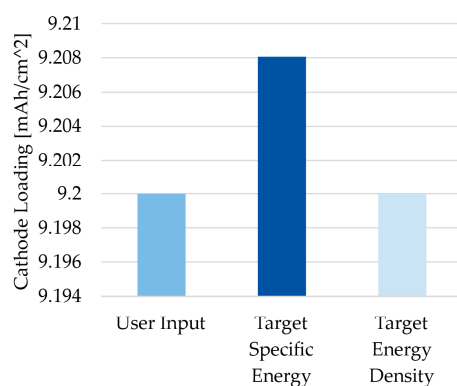


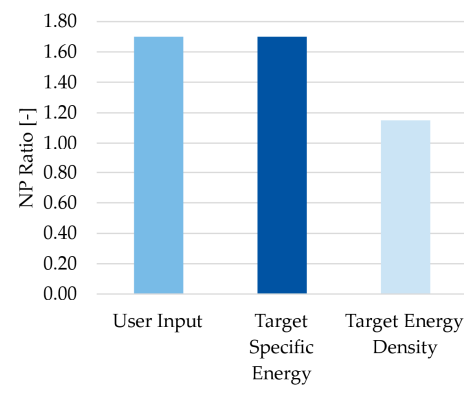
Figure 11. Optimised QS3 cell concept with adjusted cathode loading and electrolyte thickness based on sensitivity analysis with 5% KPI improvement target. The different cell layers are described in Figure 3a.

Parameter and Sensitivity Factors	E_{Grav} Optimisation	E_{Vol} Optimisation
N/P Ratio	1.7	1.149
SF: N/P	0	-0.272
Cathode Loading	9.2	34
SF: Cathode Loading	0.304	0
Electrolyte Thickness	22.07	34
SF: Electrolyte Thickness	-0.286	0

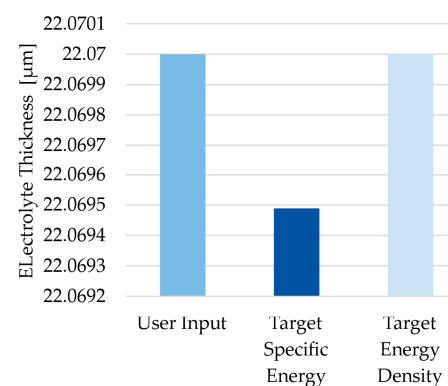
a)



c)



b)



d)

Figure 12. Sensitivity analyses of the PL2 concept with 4% and 10% KPI improvement targets. (a) Optimised parameters and their corresponding sensitivity factors (SFs) from the conducted SAs. (b) Comparison of the initial and optimised N/P ratio to achieve 4% KPI improvement target. (c) Comparison of the initial and optimised cathode loading to achieve the 10% KPI improvement target. (d) Comparison of the initial and optimised electrolyte thickness to achieve the 10% KPI improvement target.

The findings indicate that while minor adjustments to the N/P ratio effectively enhance volumetric energy density, significant modifications to cathode loading and electrolyte thickness are required to achieve meaningful improvements in gravimetric energy density.

Optimisation efforts led to improvements of +21.55% in gravimetric energy density and +8.53% in volumetric energy density. The optimisation process demonstrated that prioritising adjustments to the most sensitive parameters first allows for more efficient performance enhancement. Figure 13 illustrates the optimised values achieved for the PL2 cell concept.

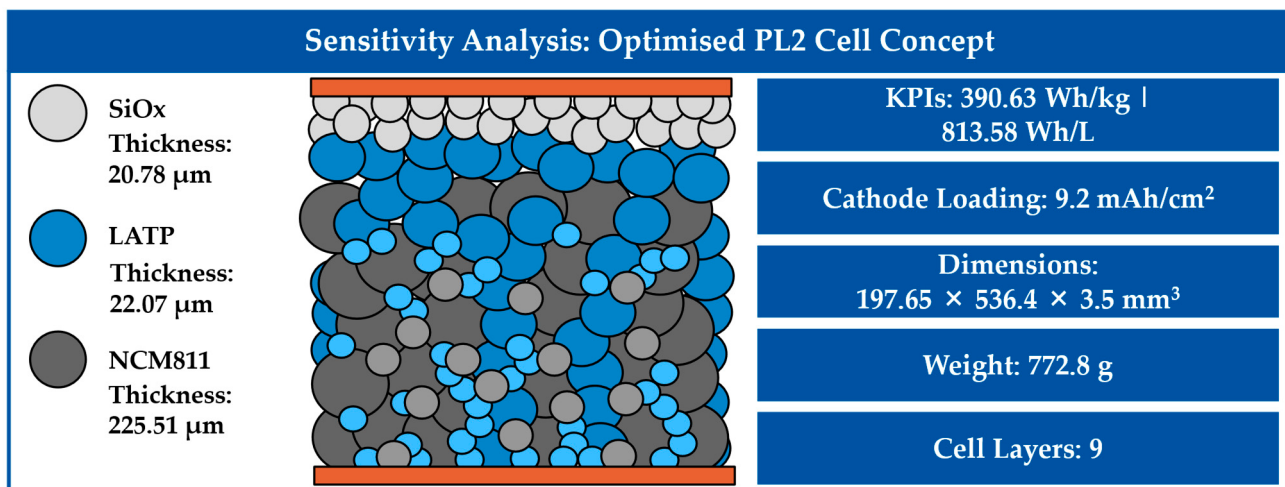


Figure 13. Optimised PL2 cell concept with adjusted N/P ratio, cathode loading, and electrolyte thickness based on sensitivity analyses with 4% and 10% KPI improvement targets. The different cell layers are described in Figure 3a.

4. Discussion and Conclusions

This study builds on and extends previous research in the field of SSB model-based design. Its primary aim was to address the limitations of existing frameworks, particularly SolidPAC, which remains the only empirical design and estimation model currently available [12]. The model developed in this work represents an improvement, offering a user-friendly, consistent, adaptable, and comprehensible toolkit. This framework enables users to optimise SSB designs by providing enhanced flexibility to explore various design parameters and configurations, with a focus on both performance metrics and practical constraints. In addition, functionalities such as compatibility validation and SA enable users to further investigate the field of SSB design.

The validation process in this study rigorously evaluated the model's performance in three key areas: predictive accuracy, functionality as a design tool, and its ability to optimise battery configurations through SA. These steps were essential for establishing the model's applicability in research and development contexts for SSBs.

The model's accuracy was evaluated by comparing its predictions to experimental results reported in the literature and benchmarking them against a validated existing design framework. The alignment of KPIs, such as gravimetric and volumetric energy densities, demonstrated the model's ability to reliably replicate experimental outcomes, with deviations of less than ±4% in most cases. However, a notable exception was observed in the comparison of gravimetric energy density with Dixit et al. [12], where a deviation of approximately −11.52% was identified. The observed discrepancy in gravimetric energy density is largely attributed to differences in mass calculation approaches, as SolidPAC applies a different method for accounting for the CC mass, which may influence the final energy density estimation [12].

It is important to acknowledge that many design parameters were approximated through calculations due to the limited availability of explicitly reported values. Consequently, the precision of the model's accuracy cannot be conclusively determined. This limitation underscores the challenges inherent in validating a model against experimental

designs with partially disclosed data, a challenge also noted in other studies [11,12,46]. Therefore, experimental validation is essential to fully assess the model's accuracy and gain deeper insights into its precision and practical applicability.

Despite these limitations, the approximated values were refined to align with the reported parameters and KPIs, ensuring a rigorous validation approach. The toolkit enables comprehensive adjustments to a wide range of design parameters and material data, allowing the user to systematically explore and perform precise calibration.

The developed model's functionality as a design tool in the early stages of battery development has been demonstrated through its application in reverse-engineering commercial SSB concepts. By utilising the model's reliability and adaptability, various design pathways were explored using publicly available data from leading SSB developers, such as QuantumScape and ProLogium. However, the reported values could not be fully reproduced by the model, highlighting the challenges of accurately modelling and validating commercial designs when key parameters are undisclosed. Nevertheless, with the available limited information, reasonable approximations to the reported values were achieved.

This highlights the model's capability to support informed decision-making during the conceptualisation and optimisation phases of battery development. This is particularly valuable in the pre-development phase, where battery concept requirements and definitions remain unclear, or experimental data are limited or incomplete. Although reverse-engineering does not fully capture the iterative and dynamic nature of battery development, it provides a valuable means to evaluate the model's applicability [54].

The integrated SA function enhances the model's effectiveness in SSB design and optimisation by systematically varying key parameters to provide insights into their impact on KPIs. Its application to the QS3 and PL2 designs demonstrated the model's capability in refining design parameters, leading to improved energy densities for both designs. However, as observed with the PL2 design, multiple SA iterations may be required since it evaluates individual parameter effects rather than their combined influence [69].

In the current model version, adjustable parameters are limited to cathode loading, electrolyte thickness, and N/P ratio. Nonetheless, the SA function enables targeted adjustments to improve cell performance and evaluate various performance improvement targets while accounting for practical design constraints. Furthermore, it can balance trade-offs between conflicting performance metrics by analysing the sensitivity factors of the parameters and adjusting according to their impact.

The limitations of the developed SSB design model primarily stem from the scope of its assumptions and simplifications. For instance, the voltage and resistance calculations are based on simplified assumptions that do not fully capture variations in SOC, temperature dependencies, or the electrical conductivity of electrodes. Another key limitation is the lack of influence of design parameters, such as cathode composition and porosity, on the modelling results. Although the model allows for adjustments to these parameters, their impact on electrochemical performance is not fully accounted for [68,70,71]. While these simplifications enhance computational efficiency and usability, they also affect the accuracy of performance predictions [72,73].

Despite these limitations, the model remains valuable in the early stages of battery concept definition and design. Its ability to quickly evaluate potential material combinations and configurations makes it an effective tool for guiding initial design decisions before conducting more detailed simulations or experimental validation. When used in conjunction with high-fidelity multiphysics models, the framework can bridge the gap between concept development and implementation, accelerating the SSB development process.

Additionally, the model has applications beyond academic research, offering commercial SSB developers, original equipment manufacturers, and related industries a practical

tool to assess the feasibility and performance potential of various SSB materials and configurations [74]. By offering a structured approach to design evaluation, the model aids in scaling up by identifying optimal material and design combinations prior to extensive prototyping. This capability may contribute to the industrialisation process by offering insights that could aid in cell manufacturing and support the transition from laboratory-scale concepts to commercial production [8,12–14].

Future refinements should aim to enhance the model's applicability by expanding its scope to include in-depth module and pack design, as well as incorporating additional parameters into the SA. Broadening the range of estimated KPIs—such as charging capabilities and cost estimation, similar to the functionality provided by BatPAC—could improve the model's comprehensiveness, making it a more versatile tool for both academic and industrial stakeholders [21].

Supplementary Materials: The following supporting information can be downloaded at: <https://www.mdpi.com/article/10.3390/batteries11040153/s1>.

Author Contributions: Conceptualisation, F.M. and J.F.P.; methodology, F.M.; software, F.M.; validation, F.M.; formal analysis, F.M.; investigation, F.M.; resources, J.F.P.; data curation, F.M.; writing—original draft preparation, F.M.; writing—review and editing, J.F.P. and F.M.; visualisation, F.M.; supervision, J.F.P.; project administration, J.F.P., S.W., H.B., H.H.H. and A.K.; funding acquisition, J.F.P., S.W., H.B., H.H.H. and A.K. All authors have read and agreed to the published version of the manuscript.

Funding: This research was funded by the German Federal Ministry of Education and Research under grant number 03XPO590E.

Data Availability Statement: The original contributions presented in this study are included in the article and Supplementary Materials. Further inquiries can be directed to the corresponding author.

Acknowledgments: The research project “FoFeBat 4”, on which this publication is based, was funded by the German Federal Ministry of Education and Research. In FoFeBat 4, the project team investigates alternative manufacturing processes and technologies for solid-state batteries, scales material synthesis, processes solid electrolytes, and analyses operating conditions and safety aspects in cell operation.

Conflicts of Interest: The authors declare no conflicts of interest.

Appendix A

Table A1. Anode active material data.

Anode Active Material	Specific Capacity * [mAh/g]	Molecular Weight [g/mol]	Material Density * [g/cm ³]
Lithium metal (Li-metal)	3860	6.94	0.534
Graphite	360	12.01	2.26
Silicon (SiO _x)	3579	28.08	2.33
Anode-free design	3860	6.94	0.534

* Unless otherwise stated, all material property data used in the model are derived from experimental measurements reported in the literature and correspond to room temperature (approximately 25 °C) and atmospheric pressure (approximately 1 bar) conditions.

Table A2. Cathode active material data.

Cathode Active Material	Specific Capacity * [mAh/g]	Molecular Weight [g/mol]	Material Density * [g/cm ³]	OCV at 20–100% SOC * [V]
NMC811	210	95	4.65	3.565–4.2
NMC622	180	94.39	4.65	3.565–4.2

Table A2. *Cont.*

Cathode Active Material	Specific Capacity * [mAh/g]	Molecular Weight [g/mol]	Material Density * [g/cm ³]	OCV at 20–100% SOC * [V]
NMC333	155	93.88	4.65	3.516–4.1
NCA	200	96.1	4.78	3.551–4.1
LFP	150	157.76	3.45	3.246–3.8
LMO	108	176.02	4.23	2.408–2.66
LNMO	115	660.3	3.1	4.75–4.95
NMC/75% LMO	113.8	155.5	4.34	2.7–4.1
LCO	150	97.87	5.05	3.75–4.2
S	1675	32	2.07	2.1–2.5
Li ₃ V ₂ (PO ₄) ₃	197	407.62	2.89	3.6–4.2

* Unless otherwise stated, all material property data used in the model are derived from experimental measurements reported in the literature and correspond to room temperature (approximately 25 °C) and atmospheric pressure (approximately 1 bar) conditions.

Table A3. Solid electrolyte material data.

Solid Electrolyte Materials	Ionic Conductivity * [mS/cm]	Molecular Weight [g/mol]	Material Density * [g/cm ³]	AAM SE Interfacial Resistance * [Ω cm ²]	CAM SE Interfacial Resistance * [Ω cm ²]
LLZO	0.5	839.74	5.2	100	200
LATP	1	380.62	2.92	50	300
LPS	1	180.05	1.83	50	200
LGPS	12	588.69	2	10	50
LPSCI	1	268.4	1.54	50	200
LiTFSI	0.001	287.075	1.33	100	400
Li ₃ InCl ₆	1	348.35	2.59	50	200
LiPON	0.001	115.79	2.3	50	500
LMZP	0.001	287.075	1.12	50	400
PEO-LiTFSI	0.001	287.075	1.12	50	400
PEO-LLZO	0.001	369.91	1.26	50	400

* Unless otherwise stated, all material property data used in the model are derived from experimental measurements reported in the literature and correspond to room temperature (approximately 25 °C) and atmospheric pressure (approximately 1 bar) conditions.

Appendix B

Table A4. Cell configuration and dimension data for accuracy validation of the model with Dixit et al. [12].

Cell Configuration and Dimensions	Dixit et al. [12]	PEM-Model
Cell chemistry (anode solid electrolyte catholyte–anode)	Li LLZO LLZO–NMC622	
Target energy of cell [kWh]	0.2426 *	0.231
Stacking and coating configuration	Bipolar stacking and bilayer coating	
Number of layers in a cell stack	194 *	
Cathode composition (active material, catholyte, carbon, binder) [wt%]	80:10:5:5	
N/P ratio	1.2	
Electrolyte thickness [μm]	25	
Anode thickness [μm]	3.42 *	
Cathode thickness [μm]	60.5	
Cathode active material areal loading [mAh/cm ²]	3	
Target cell thickness [mm]	20	

* Values are not reported by Dixit et al. [12] but are calculated with SolidPAC.

Table A5. Cell configuration and dimension data for accuracy validation of model with Tan et al. [47].

Cell Configuration and Dimensions	Tan et al. [47]	PEM-Model
Cell chemistry (anode solid electrolyte catholyte–cathode)	Si LiPSCl LPSCl–NCM622	
Target energy of cell [Wh]	11.64 *	
Stacking and coating configuration	Conventional stacking and single-layer coating	
Number of layers in a cell stack	20	
Cathode composition (active material, catholyte, carbon, binder) [wt%]	80:16:5:3:0.5 **	
N/P ratio	1.1	
Electrolyte thickness [μm]	30	
Anode thickness [μm]	13.5	10.11
Cathode thickness [μm]	120	139.87
Cathode active material areal loading [mAh/cm ²]	6	
Target cell thickness [mm]	4.19	

* Values are calculated or approximated to achieve alignment with cell dimensions. ** Values are adjusted from the reported 80:19.5:3:0.5 composition.

Table A6. Cell configuration and dimension data for accuracy validation of model with Nam et al. [48].

Cell Configuration and Dimensions	Nam et al. [48]	PEM-Model
Cell chemistry (anode solid electrolyte catholyte–cathode)	Graphite LiPSCl LiPSCl–NCM811	
Target energy of cell [Wh]	0.433 *	
Stacking and coating configuration	Conventional stacking and single-layer coating	
Number of layers in a cell stack	1	
Cathode composition (active material, catholyte, carbon, binder) [wt%]	68.1:29.2:1.3:1.4	
N/P ratio	1.71 *	
Electrolyte thickness [μm]	30	
Anode thickness [μm]	65	65.01
Cathode thickness [μm]	88	88.59
Cathode active material areal loading [mAh/cm ²]	2.32 *	
Target cell thickness [mm]	0.9 *	

* Values are calculated or approximated to achieve alignment with cell dimensions.

Table A7. Cell configuration and dimension data for design validation of QuantumScape’s QSE-5B prototype.

Cell Configuration and Dimensions	QuantumScape	PEM-Model
Cell chemistry (anode SE catholyte–cathode)	Anode-free ceramic-SE gel-ceramic-SE-LFP/NCM	Anode-free ceramic-SE ceramic-SE-LFP/NCM
Target energy of cell [Wh]	21.6	
Nominal voltage [V]	3.84	cf. Figure 5
Stacking and coating configuration	Bipolar stacking and single-layer coating	
Number of layers in a cell stack	24	
Cell mass [g]	71.8	
Cell dimensions [mm ²]	84.5 × 65.6	
Cathode composition (active material, catholyte, carbon, binder) [wt%]	n/a	cf. Table 6
N/P ratio	1	
Electrolyte thickness [μm]	n/a	cf. Table 6
Anode thickness [μm]	0	
Cathode thickness [μm]	n/a	cf. Figure 5
Cathode active material areal loading [mAh/cm ²]	6.2 *	
Target cell thickness [mm]	4.6	

* Values are calculated or approximated to achieve alignment with cell dimensions.

Table A8. Cell configuration and dimension data for design validation of ProLogium's LLCB206560 prototype.

Cell Configuration and Dimensions	ProLogium	PEM-Model
Cell chemistry (anode SE catholyte–cathode)	SiOx ceramic–SE ceramic–SE–NCM811	
Target energy of cell [Wh]	280	
Nominal voltage [V]	3.42	
Stacking and coating configuration	Bipolar stacking and single-layer coating	
Number of layers in a cell stack	n/a	cf. Figure 8
Cell mass [g]	961	
Cell dimensions [mm ²]	560 × 206	
Cathode composition (active material, catholyte, carbon, binder) [wt%]	n/a	cf. Table 7
N/P ratio	n/a	cf. Table 7
Electrolyte thickness [μm]	n/a	cf. Table 7
Anode thickness [μm]	n/a	cf. Figure 8
Cathode thickness [μm]	n/a	cf. Figure 8
Cathode active material areal loading [mAh/cm ²]	n/a	cf. Table 7
Target cell thickness [mm]	3.5	

References

- IRENA. *World Energy Transitions Outlook 2023: 1.5 °C Pathway*; International Renewable Energy Agency: Masdar City, Abu Dhabi, 2023; pp. 1–258.
- Ouyang, D.; Liu, B.; Huang, J.; Wang, Z. Degradation and safety performance of lithium-ion cells under high-rate charging/discharging scenarios. *Process Saf. Environ. Prot.* **2024**, *185*, 76–85. [[CrossRef](#)]
- Jaguemont, J.; Darwiche, A.; Bardé, F. Optimal Fast-Charging Strategy for Cylindrical Li-Ion Cells at Different Temperatures. Available online: <https://www.mdpi.com/2032-6653/15/8/330> (accessed on 13 November 2024).
- Zhang, Y.; Liu, H.; Xie, Z.; Qu, W.; Freschi, D.J.; Liu, J. Progress and Perspectives of Lithium Aluminum Germanium Phosphate-Based Solid Electrolytes for Lithium Batteries. *Adv. Funct. Mater.* **2023**, *33*, 2300973. [[CrossRef](#)]
- Polu, A.R.; Kim, K.; Kareem, A.A.; Kim, D.; Song, S.; Savilov, S.V.; Singh, P.K. Impact of tetracyanoethylene plasticizer on PEO based solid polymer electrolytes for improved ionic conductivity and solid-state lithium-ion battery performance. *J. Power Sources* **2025**, *625*, 235742. [[CrossRef](#)]
- Wu, J.; Li, J.; Yao, X. Exploring the Potential of Halide Electrolytes for Next-Generation All-Solid-State Lithium Batteries. *Adv. Funct. Mater.* **2024**, *35*, 2416671. [[CrossRef](#)]
- Plumeyer, J.F.; Heimes, H.; Kampker, A.; Wennemar, S.; Scheibe, A.; Michaelis, S.; Schütrumpf, J. *Production of an All-Solid-State Battery Cell*; PEM of RWTH: Aachen, Germany, 2023; pp. 1–24.
- Schmaltz, T.; Hartmann, F.; Wicke, T.; Weymann, L.; Neef, C.; Janek, J. A Roadmap for Solid-State Batteries. *Adv. Energy Mater.* **2023**, *13*, 2301886. [[CrossRef](#)]
- Ahmad, N.; Fan, C.; Faheem, M.; Liang, X.; Xiao, Y.; Cao, X.; Zeng, C.; Dong, Q.; Yang, W. Key challenges and advancements toward fast-charging all-solid-state lithium batteries. *Green Chem.* **2024**, *26*, 9529–9553. [[CrossRef](#)]
- Li, C.; Wang, Z.; He, Z.; Li, Y.; Mao, J.; Dai, K.; Yan, C.; Zheng, J. An advance review of solid-state battery: Challenges, progress and prospects. *Sustain. Mater. Technol.* **2021**, *29*, e00297. [[CrossRef](#)]
- Randau, S.; Weber, D.A.; Kötz, O.; Koerver, R.; Braun, P.; Weber, A.; Ivers-Tiffée, E.; Adermann, T.; Kulisch, J.; Zeier, W.G.; et al. Benchmarking the performance of all-solid-state lithium batteries. *Nat. Energy* **2020**, *5*, 259–270. [[CrossRef](#)]
- Dixit, M.; Parejiya, A.; Essehli, R.; Muralidharan, N.; Haq, S.U.; Amin, R.; Belharouak, I. SolidPAC is an interactive battery-on-demand energy density estimator for solid-state batteries. *Cell Rep. Phys. Sci.* **2022**, *3*, 100756. [[CrossRef](#)]
- Pang, M.-C.; Yang, K.; Brugge, R.; Zhang, T.; Liu, X.; Pan, F.; Yang, S.; Aguadero, A.; Wu, B.; Marinescu, M.; et al. Interactions are important: Linking multi-physics mechanisms to the performance and degradation of solid-state batteries. *Mater. Today* **2021**, *49*, 145–183. [[CrossRef](#)]
- Pasta, M.; Armstrong, D.; Brown, Z.L.; Bu, J.; Castell, M.R.; Chen, P.; Cocks, A.; Corr, S.A.; Cussen, E.J.; Darnbrough, E.; et al. 2020 roadmap on solid-state batteries. *J. Phys. Energy* **2020**, *2*, 32008. [[CrossRef](#)]
- Scheller, M.; Durdel, A.; Frank, A.; Kriegler, J.; Jossen, A. Impact of Polymer Interlayers on All-Solid-State Battery Performance Using a Physicochemical Modeling Approach. *J. Electrochem. Soc.* **2024**, *171*, 20509. [[CrossRef](#)]

16. Akasapu, U.; Hehenberger, P. A design process model for battery systems based on existing life cycle assessment results. *J. Clean. Prod.* **2023**, *407*, 137149. [[CrossRef](#)]
17. Cooper, R.G.; Edgett, S.J.; Kleinschmidt, E.J. *Portfolio Management for New Products*, 2nd ed.; Basic Books: New York, NY, USA, 2001; ISBN 0738205141.
18. Santos, K.; Loures, E.; Piechnicki, F.; Canciglieri, O. Opportunities Assessment of Product Development Process in Industry 4.0. *Procedia Manuf.* **2017**, *11*, 1358–1365. [[CrossRef](#)]
19. Browning, T.R.; Fricke, E.; Negele, H. Key concepts in modeling product development processes. *Syst. Eng.* **2006**, *9*, 104–128. [[CrossRef](#)]
20. Zhang, S.; Ma, J.; Dong, S.; Cui, G. Designing All-Solid-State Batteries by Theoretical Computation: A Review. *Electrochem. Energy Rev.* **2023**, *6*, 4. [[CrossRef](#)]
21. Knehr, K.; Kubal, J.; Nelson, P.; Ahmed, S. *Battery Performance and Cost Modeling for Electric-Drive Vehicles (A Manual for BatPaC v5.0)*; Argonne National Laboratory: Lemont, IL, USA, 2022. [[CrossRef](#)]
22. Zanabria, C.; Andrén, F.; Kathan, J.; Strasser, T. Rapid Prototyping of Multi-Functional Battery Energy Storage System Applications. *Appl. Sci.* **2018**, *8*, 1326. [[CrossRef](#)]
23. Camburn, B.; Dunlap, B.; Gurjar, T.; Hamon, C.; Green, M.; Jensen, D.; Crawford, R.; Otto, K.; Wood, K. A Systematic Method for Design Prototyping. *J. Mech. Des.* **2015**, *137*, 081102. [[CrossRef](#)]
24. Bistri, D.; Afshar, A.; Di Leo, C.V. Modeling the chemo-mechanical behavior of all-solid-state batteries: A review. *Meccanica* **2021**, *56*, 1523–1554. [[CrossRef](#)]
25. Tamilselvi, S.; Gunasundari, S.; Karuppiah, N.; Razak RK, A.; Madhusudan, S.; Nagarajan, V.M.; Sathish, T.; Shamim, M.Z.M.; Saleel, C.A.; Afzal, A. A Review on Battery Modelling Techniques. *Sustainability* **2021**, *13*, 10042. [[CrossRef](#)]
26. Fu, Z.-H.; Chen, X.; Zhang, Q. Review on the lithium transport mechanism in solid-state battery materials. *WIREs Comput. Mol. Sci.* **2023**, *13*, e1621. [[CrossRef](#)]
27. Li, G.; Fan, G.; Zhang, X.; Han, J.; Wang, Y.; Liu, Y.; Jia, L.; Guo, B.; Zhu, C.; He, M. Modeling of an all-solid-state battery with a composite positive electrode. *eTransportation* **2024**, *20*, 100315. [[CrossRef](#)]
28. Sangrós Giménez, C.; Helmers, L.; Schilde, C.; Diener, A.; Kwade, A. Modeling the Electrical Conductive Paths within All-Solid-State Battery Electrodes. *Chem. Eng. Technol.* **2020**, *43*, 819–829. [[CrossRef](#)]
29. Vadhva, P.; Boyce, A.M.; Hales, A.; Pang, M.-C.; Patel, A.N.; Shearing, P.R.; Offer, G.; Rettie, A.J.E. Towards Optimised Cell Design of Thin Film Silicon-Based Solid-State Batteries via Modelling and Experimental Characterisation. *J. Electrochem. Soc.* **2022**, *169*, 100525. [[CrossRef](#)]
30. Deng, Z.; Hu, X.; Lin, X.; Le, X.; Li, J.; Guo, W. A Reduced-Order Electrochemical Model for All-Solid-State Batteries. *IEEE Trans. Transp. Electrif.* **2021**, *7*, 464–473. [[CrossRef](#)]
31. Rajmakers, L.; Danilov, D.L.; Eichel, R.-A.; Notten, P. An advanced all-solid-state Li-ion battery model. *Electrochim. Acta* **2020**, *330*, 135147. [[CrossRef](#)]
32. Park, J.; Kim, K.T.; Oh, D.Y.; Jin, D.; Kim, D.; Jung, Y.S.; Lee, Y.M. Digital Twin-Driven All-Solid-State Battery: Unraveling the Physical and Electrochemical Behaviors. *Adv. Energy Mater.* **2020**, *10*, 2001563. [[CrossRef](#)]
33. Sultanova, L.; Figiel, Ł. Microscale diffusion-mechanics model for a polymer-based solid-state battery cathode. *Comput. Mater. Sci.* **2021**, *186*, 109990. [[CrossRef](#)]
34. Zhu, J.; Wierzbicki, T.; Li, W. A review of safety-focused mechanical modeling of commercial lithium-ion batteries. *J. Power Sources* **2018**, *378*, 153–168. [[CrossRef](#)]
35. Nanda, S.; Gupta, A.; Manthiram, A. Anode-Free Full Cells: A Pathway to High-Energy Density Lithium-Metal Batteries. *Adv. Energy Mater.* **2021**, *11*, 2000804. [[CrossRef](#)]
36. Jin, X.; Vora, A.; Hosking, V.; Saha, T.; Shaver, G.; García, R.E.; Wasynczuk, O.; Varigonda, S. Physically-based reduced-order capacity loss model for graphite anodes in Li-ion battery cells. *J. Power Sources* **2017**, *342*, 750–761. [[CrossRef](#)]
37. Shaheen, A.M.; Hamida, M.A.; El-Sehiemy, R.A.; Elattar, E.E. Optimal parameter identification of linear and non-linear models for Li-Ion Battery Cells. *Energy Rep.* **2021**, *7*, 7170–7185. [[CrossRef](#)]
38. Wang, X.; Wen, L.; Zheng, Y.; Liu, H.; Liang, G. Facile synthesis and electrochemical properties of high tap density LiFePO₄/C. *Ionics* **2019**, *25*, 4589–4596. [[CrossRef](#)]
39. Chang, Z.; Chen, Z.; Wu, F.; Tang, H.; Zhu, Z.; Yuan, X.; Wang, H. Synthesis and properties of high tap-density cathode material for lithium ion battery by the eutectic molten-salt method. *Solid State Ion.* **2008**, *179*, 2274–2277. [[CrossRef](#)]
40. Koerver, R.; Aygün, I.; Leichtweiß, T.; Dietrich, C.; Zhang, W.; Binder, J.O.; Hartmann, P.; Zeier, W.G.; Janek, J. Capacity Fade in Solid-State Batteries: Interphase Formation and Chemomechanical Processes in Nickel-Rich Layered Oxide Cathodes and Lithium Thiophosphate Solid Electrolytes. *Chem. Mater.* **2017**, *29*, 5574–5582. [[CrossRef](#)]
41. Schnell, J.; Günther, T.; Knoche, T.; Vieider, C.; Köhler, L.; Just, A.; Keller, M.; Passerini, S.; Reinhart, G. All-solid-state lithium-ion and lithium metal batteries—Paving the way to large-scale production. *J. Power Sources* **2018**, *382*, 160–175. [[CrossRef](#)]

42. Noelle, D.J.; Wang, M.; Le, A.V.; Shi, Y.; Qiao, Y. Internal resistance and polarization dynamics of lithium-ion batteries upon internal shorting. *Appl. Energy* **2018**, *212*, 796–808. [CrossRef]
43. Li, Z.; Fu, J.; Zhou, X.; Gui, S.; Wei, L.; Yang, H.; Li, H.; Guo, X. Ionic Conduction in Polymer-Based Solid Electrolytes. *Adv. Sci.* **2023**, *10*, e2201718. [CrossRef]
44. Luo, W.; Gong, Y.; Zhu, Y.; Li, Y.; Yao, Y.; Zhang, Y.; Fu, K.K.; Pastel, G.; Lin, C.-F.; Mo, Y.; et al. Reducing Interfacial Resistance between Garnet-Structured Solid-State Electrolyte and Li-Metal Anode by a Germanium Layer. *Adv. Mater.* **2017**, *29*, 1606042. [CrossRef]
45. Han, X.; Gong, Y.; Fu, K.K.; He, X.; Hitz, G.T.; Dai, J.; Pearse, A.; Liu, B.; Wang, H.; Rubloff, G.; et al. Negating interfacial impedance in garnet-based solid-state Li metal batteries. *Nat. Mater.* **2017**, *16*, 572–579. [CrossRef]
46. Puls, S.; Nazmutdinova, E.; Kalyk, F.; Woolley, H.M.; Thomsen, J.F.; Cheng, Z.; Fauchier-Magnan, A.; Gautam, A.; Gockeln, M.; Ham, S.; et al. Benchmarking the reproducibility of all-solid-state battery cell performance. *Nat. Energy* **2024**, *9*, 1310–1320. [CrossRef]
47. Tan, D.H.S.; Chen, Y.; Yang, H.; Bao, W.; Sreenarayanan, B.; Doux, J.; Li, W.; Lu, B.; Ham, S.; Sayahpour, B.; et al. Carbon-free high-loading silicon anodes enabled by sulfide solid electrolytes. *Am. Assoc. Adv. Sci.* **2021**, *373*, 1494–1499. [CrossRef] [PubMed]
48. Nam, Y.J.; Oh, D.Y.; Jung, S.H.; Jung, Y.S. Toward practical all-solid-state lithium-ion batteries with high energy density and safety: Comparative study for electrodes fabricated by dry- and slurry-mixing processes. *J. Power Sources* **2018**, *375*, 93–101. [CrossRef]
49. Tan, D.H.; Meng, Y.S.; Jang, J. Scaling up high-energy-density sulfidic solid-state batteries: A lab-to-pilot perspective. *Joule* **2022**, *6*, 1755–1769. [CrossRef]
50. Krauskopf, T.; Richter, F.H.; Zeier, W.G.; Janek, J. Physicochemical Concepts of the Lithium Metal Anode in Solid-State Batteries. *Chem. Rev.* **2020**, *120*, 7745–7794. [CrossRef]
51. Jeon, I.; Hong, W.G.; Yoon, S.; Choi, Y.; Kim, H.J.; Kim, J.-P. Safety, high-performing and effects of the N/P ratio of a solid lithium ion battery using PEGDME based polymer electrolytes. *Heliyon* **2023**, *9*, e13292. [CrossRef]
52. Lee, Y.-G.; Fujiki, S.; Jung, C.; Suzuki, N.; Yashiro, N.; Omoda, R.; Ko, D.-S.; Shiratsuchi, T.; Sugimoto, T.; Ryu, S.; et al. High-energy long-cycling all-solid-state lithium metal batteries enabled by silver–carbon composite anodes. *Nat. Energy* **2020**, *5*, 299–308. [CrossRef]
53. Wang, C.; Yu, R.; Duan, H.; Lu, Q.; Li, Q.; Adair, K.R.; Bao, D.; Liu, Y.; Yang, R.; Wang, J.; et al. Solvent-Free Approach for Interweaving Freestanding and Ultrathin Inorganic Solid Electrolyte Membranes. *ACS Energy Lett.* **2022**, *7*, 410–416. [CrossRef]
54. Raibulet, C.; Arcelli Fontana, F.; Zanoni, M. Model-Driven Reverse Engineering Approaches: A Systematic Literature Review. *IEEE Access* **2017**, *5*, 14516–14542. [CrossRef]
55. Taylor, E.J.; Inman, M. Looking at Patent Law: Patenting a Solid State Lithium-Metal Battery—A Case Study. *Electrochem. Soc. Interface* **2021**, *30*, 37–42. [CrossRef]
56. Pacios, R.; Villaverde, A.; Martínez-Ibañez, M.; Casas-Cabanas, M.; Aguesse, F.; Kvasha, A. Roadmap for Competitive Production of Solid-State Batteries: How to Convert a Promise into Reality. *Adv. Energy Mater.* **2023**, *13*, 2301018. [CrossRef]
57. QuantumScape. Energy Density: Inactive Materials and Packaging Efficiency. 2023. Available online: <https://www.queantscape.com/energy-density-inactive-materials-and-packaging-efficiency/> (accessed on 13 December 2024).
58. QuantumScape. A First Look at the QSE-5 B Sample. 2024. Available online: <https://www.queantscape.com/blog/a-first-look-at-the-qse-5-b-sample/> (accessed on 13 December 2024).
59. Yim, C.-H.; Houache, M.S.; Baranova, E.A.; Abu-Lebdeh, Y. Understanding key limiting factors for the development of all-solid-state-batteries. *Chem. Eng. J. Adv.* **2023**, *13*, 100436. [CrossRef]
60. Zaman, W.; Hatzell, K.B. Processing and manufacturing of next generation lithium-based all solid-state batteries. *Curr. Opin. Solid State Mater. Sci.* **2022**, *26*, 101003. [CrossRef]
61. Schnell, J.; Tietz, F.; Singer, C.; Hofer, A.; Billot, N.; Reinhart, G. Prospects of production technologies and manufacturing costs of oxide-based all-solid-state lithium batteries. *Energy Environ. Sci.* **2019**, *12*, 1818–1833. [CrossRef]
62. Balaish, M.; Gonzalez-Rosillo, J.C.; Kim, K.J.; Zhu, Y.; Hood, Z.D.; Rupp, J.L.M. Processing thin but robust electrolytes for solid-state batteries. *Nat. Energy* **2021**, *6*, 227–239. [CrossRef]
63. Bockey, G.; Plumeyer, J.F.; Wennemar, S.; Dorn, B.; Kampker, A. Comparative Analysis of Lithium Metal Anode Production Methods: Evaluating Liquid-Based Manufacturing Technology for Mass Production. In Proceedings of the 5th Conference on Production Systems and Logistics, Stellenbosch, South Africa, 14–17 November 2023.
64. Plocher, L.; Plumeyer, J.F.; Wennemar, S. Automatisierter Stapelprozess zur Herstellung von Festkörperbatterien. *Z. Für Wirtsch. Fabr.* **2022**, *117*, 570–575. [CrossRef]
65. ProLogium Technology Co., Ltd. Core Technologies—ProLogium Technology Co., Ltd. Available online: <https://prologium.com/tech/core-technology/> (accessed on 21 December 2024).
66. ProLogium Technology Co., Ltd. ProLogium 2024 Paris Motor Show Brochure—ProLogium Technology Co., Ltd. Available online: <https://prologium.com/prologium-2024-paris-motor-show/> (accessed on 21 December 2024).

67. Song, A.; Zhang, W.; Guo, H.; Dong, L.; Jin, T.; Shen, C.; Xie, K. A Review on the Features and Progress of Silicon Anodes-Based Solid-State Batteries. *Adv. Energy Mater.* **2023**, *13*, 2301464. [[CrossRef](#)]
68. Heubner, C.; Nickol, A.; Seeba, J.; Reuber, S.; Junker, N.; Wolter, M.; Schneider, M.; Michaelis, A. Understanding thickness and porosity effects on the electrochemical performance of $\text{LiNi}_{0.6}\text{Co}_{0.2}\text{Mn}_{0.2}\text{O}_2$ -based cathodes for high energy Li-ion batteries. *J. Power Sources* **2019**, *419*, 119–126. [[CrossRef](#)]
69. Więckowski, J.; Sałabun, W. Comparative Sensitivity Analysis in Composite Material Selection: Evaluating OAT and COMSAM Methods in Multi-criteria Decision-making. *Spectr. Mech. Eng. Oper. Res.* **2025**, *2*, 1–12. [[CrossRef](#)]
70. Mizuno, F.; Hayashi, A.; Tadanaga, K.; Tatsumisago, M. Effects of Conductive Additives in Composite Positive Electrodes on Charge-Discharge Behaviors of All-Solid-State Lithium Secondary Batteries. *J. Electrochem. Soc.* **2005**, *152*, A1499. [[CrossRef](#)]
71. Hayakawa, E.; Nakamura, H.; Ohsaki, S.; Watano, S. Design of active-material/solid-electrolyte composite particles with conductive additives for all-solid-state lithium-ion batteries. *J. Power Sources* **2023**, *555*, 232379. [[CrossRef](#)]
72. Khalik, Z.; Bergveld, H.J.; Donkers, M. On Trade-offs Between Computational Complexity and Accuracy of Electrochemistry-based Battery Models. In Proceedings of the 2019 IEEE 58th Conference on Decision and Control (CDC), Nice, France, 11–13 December 2019; IEEE: Piscataway, NJ, USA, 2019; pp. 7740–7745, ISBN 978-1-7281-1398-2.
73. Khalik, Z.; Donkers, M.; Bergveld, H.J. Model simplifications and their impact on computational complexity for an electrochemistry-based battery modeling toolbox. *J. Power Sources* **2021**, *488*, 229427. [[CrossRef](#)]
74. Heimes, H.; Kampker, A.; Frank, M.; Plumeyer, J.F.; Scheibe, A. *Battery Atlas 2024 (2nd Edition)—Shaping the European Lithium-ion Battery Industry*; PEM of RWTH Aachen: Aachen, Germany, 2024; ISBN 978-3-947920-33-4.

Disclaimer/Publisher’s Note: The statements, opinions and data contained in all publications are solely those of the individual author(s) and contributor(s) and not of MDPI and/or the editor(s). MDPI and/or the editor(s) disclaim responsibility for any injury to people or property resulting from any ideas, methods, instructions or products referred to in the content.